Shape Memory Alloy Rotary Actuator for CubeSat Deployable Structures

by

Katherine S. Chun

B.S., University of Washington (2018)

Submitted to the Department of Aeronautics and Astronautics
in partial fulfillment of the requirements for the degree of

Master of Science in Aeronautics and Astronautics

at the

MASSACHUSETTS INSTITUTE OF TECHNOLOGY

June 2020

Author .....
Department of Aeronautics and Astronautics
May 19, 2020

Certified by .....
Kerri Cahoy
Associate Professor of Aeronautics and Astronautics
Thesis Supervisor

Accepted by .....
Sertac Karaman
Associate Professor of Aeronautics and Astronautics
Chairman, Graduate Program Committee

Shape Memory Alloy Rotary Actuator for CubeSat Deployable Structures

by

Katherine S. Chun

Submitted to the Department of Aeronautics and Astronautics
on May 19, 2020, in partial fulfillment of the
requirements for the degree of
Master of Science in Aeronautics and Astronautics

Abstract

Small satellites have lowered the barrier to entry for space-bound science and technology demonstrations. However, the small form factor requires extremely low size, weight, and power for any on-board hardware. Precision actuation of deployable structures has previously been achievable only through low SWaP single-use actuators or motor-driven, high SWaP multiple-use actuators. The Folded Lightweight Actuated Positioning System has the potential to provide an ultra-lightweight multiple-use actuator by using a Joule-heated shape memory alloy-based hinge. The hinge uses two shape memory alloy strips which are trained in opposite directions and mounted into a rotary actuator. Two different shape memory alloy geometries are explored: a rectangular cross-section and a circular cross-section. The rectangular hinge actuates over a range of $\pm 20^\circ$ with an average power of 0.14 W. The circular hinge actuates over a range of $\pm 23^\circ$ with an average power of 0.073 W. A closed-loop controller uses pulse width modulation and encoder measurements to actuate the rectangular hinge to within 2° of the desired angle.

Thesis Supervisor: Kerri Cahoy
Title: Associate Professor of Aeronautics and Astronautics

Acknowledgments

This thesis would not have been possible without the guidance of Professor Kerri Cahoy and the community that she has built in STAR Lab.

I would like to thank the members of the FLAPS team, both past and present. Christian Haughwout stands out as the originator of the FLAPS concept and a mentor for the many iterations of the FLAPS hinge. I would also like to acknowledge Maxim Khatsenko for his previous work on the FLAPS hinge. In the current iteration of the FLAPS hinge, I would like to thank Paula do Vale Pereira, Mario Contreras, Charles Lindsay, Shreeyam Kacker, Ethan Sit, Joseph Ward, Ronak Roy, Raul Largaespada, and Raymond Huffman for working with me over the past two years. From sponsor demonstrations to ZeroG flights, this team has continually impressed me with their dedication and enthusiasm that has enabled us to progress this far. This work has been supported by The Aerospace Corporation with the collaboration of the iLab.

I would also like to acknowledge the fabrication facilities that have made the FLAPS hinge a reality. Thank you to the MIT Glass Lab, the MIT Hobby Shop, the Project Manus Makerspaces, the Gelb Shop, and the SSL. Their generosity with their time and equipment have been invaluable.

Finally, I would like to thank my family, friends, and FGC for their constant support and encouragement through this process. Thank you to my father Craig, my mother Gladys, and my sister Emily for always believing in me.

THIS PAGE INTENTIONALLY LEFT BLANK

Contents

List of Figures

List of Tables

THIS PAGE INTENTIONALLY LEFT BLANK

Chapter 1

Introduction

Small satellites have increased accessibility to space over the last decade. CubeSats are a particularly popular form factor due to their standardized size and use of commercial off-the-shelf (COTS) components. The CubeSat form factor represents more than 90% of all nanosatellites launched [1]. The movement away from custom, one-off satellite development has greatly decreased the cost and complexity of each CubeSat. This makes them well-suited for technology demonstration missions, increasing the technology readiness level (TRL) of components prior to flying on larger missions. CubeSats are often used for science missions as well, exchanging a smaller scope for lower costs and faster development cycles.

However, CubeSats are often limited in scope due to lower size, weight, and power (SWaP) constraints. This necessitates miniaturization of nearly all on-board parts in order to maximize the science and technology return of each mission. Current in-space actuators tend to be either small, lightweight, and single actuation, or larger, more complex, and repeatable. This thesis aims to enable future CubeSat science and technology demonstration missions by developing an actuator that is simultaneously small, lightweight, and repeatable.

1.1 CubeSat Overview

Originally developed by the California Polytechnic State University in San Luis Obispo (Cal Poly), CubeSats are measured in units (Us) of 10 cm x 10 cm x 10 cm with a maximum mass of 1.33 kg per unit. A 1U CubeSat is shown in Figure 1-1. Multiple Us can be stacked together into larger rectangular structures, commonly in integers of 1U, 2U, 3U, and 6U [2].

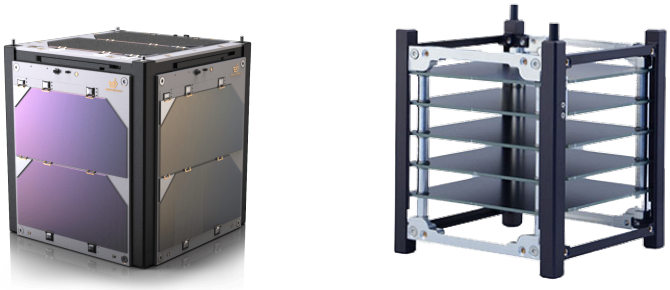

Figure 1-1: 1U CubeSat: Exterior and interior with PCB stack [3, 4].

The rigid edges of the rectangular CubeSat are called rails, which typically provide structure along the length of the satellite. The faces of the box are enclosed with flat panels that protect the interior of the CubeSat, allowing cutouts for instruments which need visibility to the exterior environment. Printed circuit boards (PCBs) are often stacked longitudinally along the length of the CubeSat body, shown in Figure 1-1. The top and bottom of the CubeSat are usually protected with caps to fully enclose the satellite.

Availability of COTS parts allows satellite engineers to design as much or as little of their CubeSat as desired. For example, a fully-assembled Blue Canyon Technologies CubeSat bus would only require the development of a payload [5]. Alternatively, each individual component could be ordered and integrated by the CubeSat engineers themselves. Major components would include a structure, thermal system, power system, communications system, attitude determination and control system, command and data handling system, and payload [6]. The move towards standardizing mechanical and electrical interfaces also allows CubeSat designers to integrate a custom selection of plug-and-play components.

Standardized CubeSat size and mass allows for launch and deployment containers to be standardized as well, further decreasing the cost of integration into launch vehicles and custom deployment methods. CubeSats are practical secondary payloads due to their small size and ability to fit in the unoccupied space within a payload fairing. Poly-Picosatellite Orbital Deployers (P-POD), shown in Figure 1-2, were developed by Cal Poly to deploy CubeSats up to 3U in length directly from a launch vehicle [2]. CubeSats with a target altitude of approximately 400 km can also be flown on cargo resupply missions and deployed from the International Space Station (ISS) [2]. The ISS has been outfitted with Nanoracks CubeSat Deployers (NRCSD), shown in Figure 1-2, to deploy CubeSats up to 6U in length, creating additional opportunities for deployment beyond individual launch vehicle timelines [7]. A majority of dispensers are secure containers with electrically actuated doors that open and eject the CubeSat into space.

Figure 1-2: CubeSat dispensers. Left: P-POD CubeSat dispenser developed by Cal Poly. Right: NRCSD CubeSat dispenser developed by NanoRacks [8, 7].

CubeSats are well-suited for technology demonstrations due to their rapid development cycles and lower cost requirements. They typically house one to three scientific instruments as their primary payload. The lower barrier to entry has enabled academic institutions as well as smaller commercial entities to launch and operate their own satellites. As a whole, this class of nanosatellites is well positioned to make quick, incremental progress in space-based science and technology objectives.

1.2 Deployable Structures on CubeSats

Deployable structures are a popular approach for working beyond the standard CubeSat size constraints. Deployables are stowed within the volume limitations imposed by the CubeSat standard and dispenser requirements, then expand to a larger size once in orbit. Typical CubeSat deployables include solar panels, antennas, and payloads [9].

There is an important distinction between single-use and repeatable deployable structures. Single-use refers to deployables which are stowed on launch and actuated to their full size for the remainder of the mission. Solar panels and antennas have historically been single-use deployables, using mechanisms such as burn wires, spring-loaded hinges, and latches. Some examples are Clyde Space's single-deployed and double-deployed 3U COTS solar panels, which use thermal knives to actuate spring-loaded hinges [10]. Locking mechanisms are then used to maintain final solar panel position. For antennas, Innovative Solutions in Space offers an array of monopole, dipole, and helical antennas which are mechanically and electrically actuated [11]. Both are shown in Figure 1-3.

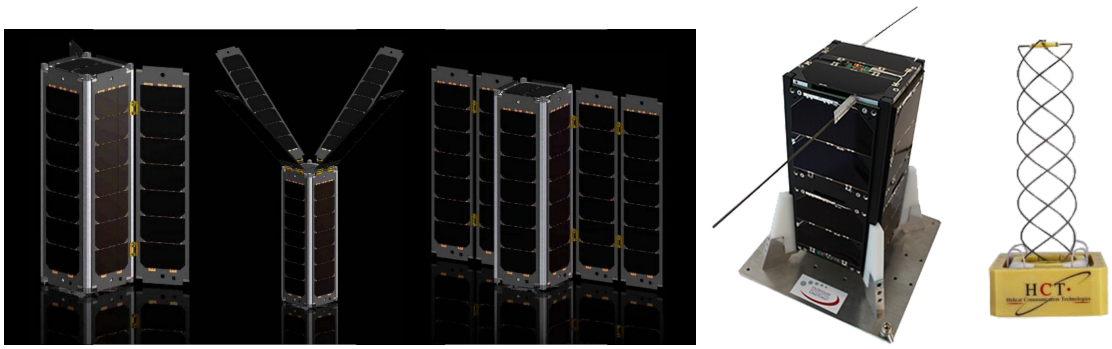

Figure 1-3: COTS single-use deployables. Left: Clyde Space solar panels [10]. Right: Innovative Solutions in Space antennas [11].

More ambitious deployable packing ratios are demonstrated as payloads on CubeSat missions. For example, the Integrated Solar Array Reflectarray (ISARA) mission has a 0.3 m x 0.3 m deployable solar array which doubles as a Ka-band high gain antenna. The 'turkey tail' panel configuration unfolds to using a spring-loaded hinge deployment mechanism adapted from the standard Pumpkin, Inc. COTS 3U so-

lar panel offerings [12]. Figure 1-4 shows a similar reflectarray design used for the MarCO CubeSats, a pair of 6U nanosatellites that provided real-time data for the Mars Insight landing. The reflectarray was made up of three 6U flat panels which deployed via spring-loaded hinges [13]. A different approach is deploying the external CubeSat structure itself, as demonstrated by the ALL-STAR CubeSat. ALL-STAR has a deployable internal Payload Extension Zone (PEZ) which is actuated via mini-Frangibolts and two constant force springs [14].

RainCube is an example of a 6U CubeSat with a 0.5 m deployable Ka-band parabolic antenna stowed within a 1.5U volume. The antenna is deployed out of the canister via lead screws, releasing a spring ring to deploy the ribs and locking in place with spring-loaded latches [15]. Another example is NanoSail-D2, a 3U CubeSat with a 10 m x 10 m solar sail stowed within a 2U volume. The sail was deployed using spooled Triangular Rollable and Collapsible (TRAC) booms. Both are shown in Figure 1-4.

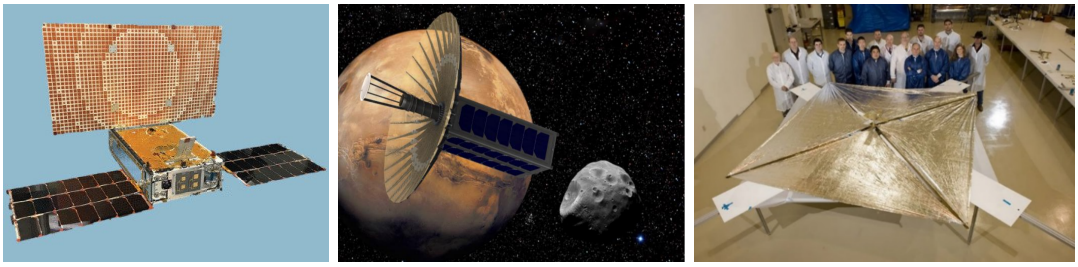

Figure 1-4: Deployable payloads on CubeSat. Left to right: MarCO, RainCube, NanoSail-D [13, 15, 16].

Booms are another CubeSat deployable which are common in both single-use and repeatable models, shown in Figure 1-5. TRAC booms are a single-deployment option consisting of two composite tape measures bonded along one edge, then flattened and rolled into a small stowing form factor. The TRAC boom was first flown on NanoSail-D and first deployed on NanoSail-D2 [17]. Oxford Space Systems' Astrotube Max can operate as a single shot, partial deployment, or fully retractable scalable boom. The Astrotube Max is flight proven on CFESat and AlSat-Nano, among other commercially integrated satellites [18, 19]. Northrop Grumman also offers a small retractable boom, the Nano Storable Tubular Extendable Member (STEM), which

is modified from the STEM deployables designed for the Hubble Space Telescope [20]. Another CubeSat deployable payload is AAReST's composite boom, which is stowed using folded tape-spring hinges and deployed in two stages via burn wire and motor-driven cable spool [21].

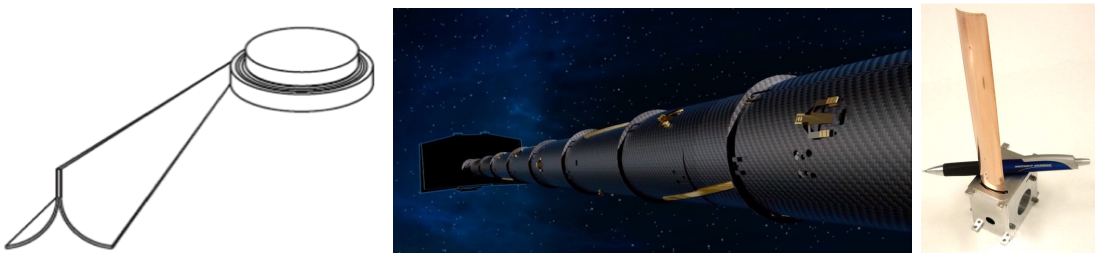

Figure 1-5: Deployable booms. Left to right: TRAC, Astrotube Max, Nano STEM [17, 19, 20].

Repeatable actuation deployables are often more complex and higher SWaP than single-use mechanisms. For example, currently available COTS actuators for repeatable solar panel actuation generally include a mechanical motor. Moog offers uniaxial and biaxial repeatable solar panel deployment via their solar array drive assemblies (SADAs). SADAs typically use slip rings to enable continuous motion, potentiometers or encoders for position feedback, and harmonic drive gear sets depending on the model [22]. Sierra Nevada Corporation offers a similar SADA model for solar array deployment and pointing. The Sierra Nevada Corporation SADA uses a stepper motor to drive a zero backlash harmonic drive and slip ring to enable continuous rotation [23].

While the previous SADAs are larger in size, Honeybee Robotics has developed an ultra-thin, low power, stackable SADA for use on CubeSats. Designed to be mounted in the 'wasted' payload space along the edges of the CubeSat caps, the Honeybee Robotics SADA uses a stepper motor and gear shaft to provide repeatable rotation [24]. MMA Design also offers a similar CubeSat-specific SADA for 3U, 6U, and 12U form factors [25]. Both CubeSat COTS SADAs are shown in Figure 1-6. Relevant specifications for all listed SADAs are outlined in Table 1.1.

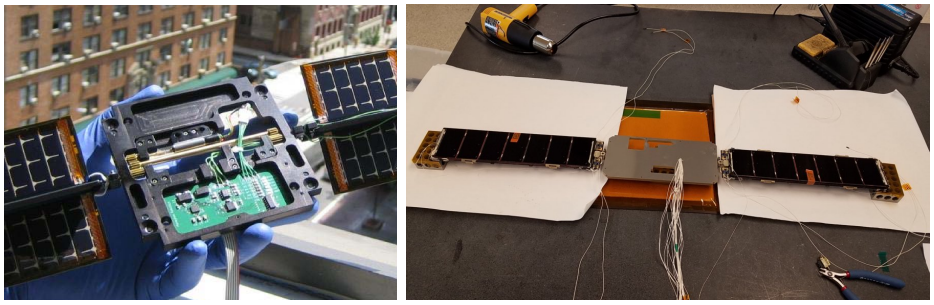

Figure 1-6: CubeSat COTS SADAs. Left: Honeybee Robotics [24]. Right: MMA Design [25].

Table 1.1: COTS SADAs

Vendor	**Model**	**Mass (g)**	**Size (cm)**
Moog [22]	Type 1	1,160	9.5⌀x 12.7
Sierra Nevada Corporation [23]	C14-750 W	1,050	8.8⌀x 12.1
MMA Design [25]	SADA	Not available	10 x 10 x 0.9
MMA Design [25]	SADA	Not available	10 x 10 x 0.65
Honeybee Robotics [24]	SADA	180	10.0 x 10.0 x 0.65

1.3 Technical Gap

The previous section outlined the difference between ultralight single-use actuators and more complex, motor-driven repeatable actuators. A representative summary of CubeSat-flown deployables are listed in Table 1.2. Single-use actuators can be reliably optimized to a few components: a stored energy mechanism, a release mechanism, and a stopping mechanism. Each actuator is typically responsible for a single action, allowing for simplicity in both the design and the potential failure modes.

Conversely, repeatable actuators are traditionally motor-driven and electrically powered. This increases the SWaP of the entire actuation system. Given the SWaP constraints of CubeSats, repeatable actuators are typically avoided unless necessary to the purpose of the mission.

Thus, there is a need for a repeatable actuator with a comparable SWaP to single-use actuators. An ultralight, compact, repeatable actuator would increase the capability of CubeSat missions without sacrificing the form factor that makes CubeSats effective.

Table 1.2: CubeSat Missions with Single-Use and Repeatable Deployable Structures

Mission	Size	Deployable	Deployment Mechanism	Use	Launch Year
QuakeSat [26]	3U	Boom-mounted magnetometer	Telescoping boom	Single use	2003
NanoSail-D2 [16]	3U	10 m x 10 m solar sail	Motor and TRAC boom assembly	Single use	2010
AENEAS [27]	3U	0.5 m deployable parabolic antenna	62 springs and a nylon burn wire	Single use	2012
ALL-STAR [14]	3U	Payload extension zone	Mini-Frangibolts and springs	Single use	2014
AlSat-Nano [28, 19, 18]	3U	Astrotube Max	Motor-driven	Repeatable	2016
ISARA [12]	3U	0.3 m x 0.3 m reflectarray	Spring-loaded hinges	Single use	2017
RainCube [15]	6U	0.5 m Ka-band parabolic deployable antenna	Motor-driven lead screws and spring-loaded latches	Single use	2018
NEA Scout [29]	6U	10 m x 10 m solar sail	Spool and TRAC boom assembly	Single use	2018
MarCO [13]	6U	0.3 m x 0.6 m reflectarray	Spring-loaded hinges	Single use	2018
FalconSat-7 [30]	3U	Telescope with diffractive optic	Precision pantograph arms	Single use	2019
OMERA [31]	6U	0.9 m x 1 m reflectarray and feed	Adjustable hinge, Tendeg motorized tape deployer and pre-loaded cables	Single use	2020 (exp)
AAReST [21]	3U	Sensor package for reconfigurable telescope	1.2 m deployable composite boom	Single use	-

1.4 Thesis Structure

Chapter 1 outlines the need for a multiple-use, repeatable, low SWaP actuator for space applications. The current state of the art is outlined and the technical gap is highlighted.

Chapter 2 looks at the advantages of shape memory alloy actuators. The selection of one-way nitinol and the original concept of FLAPS is explained.

Chapter 3 follows the development of a rotary actuator using a flat SMA plate. The design of the SMA actuator and supporting hinge structure is explained, followed by the evaluation and implementation of a controller.

Chapter 4 tracks the development of a rotary actuator using a round SMA wire. Improvements based on the limitations of the flat SMA design are incorporated. Design, manufacture, and closed loop controller evaluation of the round hinge are explained.

Chapter 5 compares the flat and round hinges with respect to actuation range, actuation time, actuation force, and closed loop step response. Both hinges are compared to the initial FLAPS hinge requirements.

Chapter 6 summarizes the findings of the thesis and outlines logical next steps for further hinge development. Potential solutions to meet full FLAPS hinge requirements are explored.

THIS PAGE INTENTIONALLY LEFT BLANK

Chapter 2

FLAPS Concept

The Folded Lightweight Actuated Positioning System (FLAPS) concept couples a rotary hinge architecture with shape memory alloys (SMAs) to achieve a small, lightweight, repeatable actuator. The ability of SMAs to actuate to multiple angles using Joule heating with minimal additional mechanisms is leveraged.

2.1 Shape Memory Alloy Overview

SMAs have the ability to return to a 'remembered' shape or size when heated above their transformation temperature. This phenomenon is enabled by the stability of the martensite phase at low temperatures and the stability of the austenite phase at high temperatures [32]. Figure 2-1 shows the transition from martensite to austenite upon heating and the return to martensite upon cooling.

Martensite has a glissile structure that can change with applied stress due to its multiple crystallographically equivalent shear directions during formation [33]. Martensite's self-accommodating (or multivariant) microstructure allows the material to accommodate strain via shearing of the crystal structure when physically deformed [34]. Detwinned martensite is formed upon deformation and twinned martensite is the self-accommodating variant that SMAs return to after cooling. Common SMAs can be elastically deformed in the martensite phase up to a strain of approximately 4% - 8%. When below maximum strain, they maintain their ability to return to their

trained austenite shape upon heating. Beyond this point, the SMA experiences non-recoverable plastic deformation [33]. Figure 2-1 shows the transition from twinned martensite to detwinned martensite upon deformation, the transition to austenite upon heating, and the transition back to twinned martensite upon cooling.

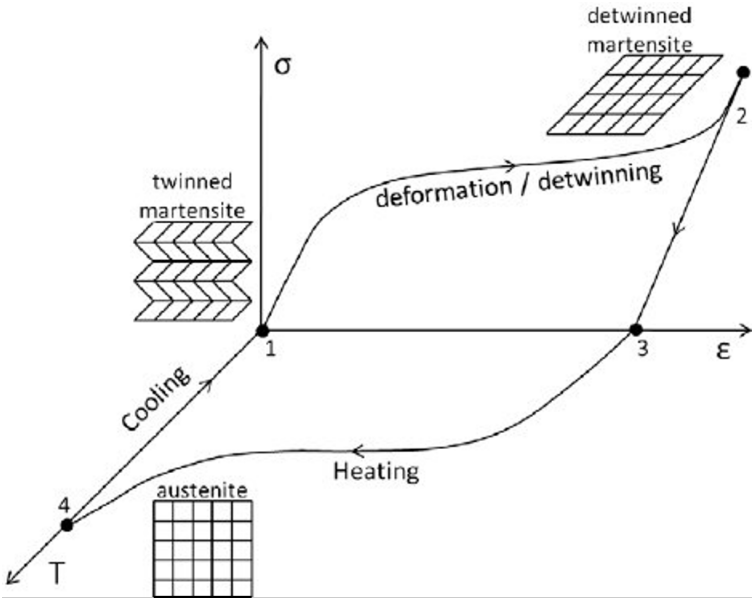

Figure 2-1: SMA transition between martensite and austenite [35].

The transition between phases occurs over a temperature range instead of at a specific transformation temperature as shown in Figure 2-2. The transformation temperature listed for SMAs is the point at which the martensite fraction passes 50% [32]. As the SMA is heated, the transition to austenite begins at the austenite start temperature (A_s) and ends at the austenite finish temperature (A_f). As the SMA cools, the transition to martensite begins at the martensite start temperature (M_s) and ends at the martensite finish temperature (M_f) [33].

Hysteresis is a measure of the temperature difference between the austenite transformation temperature during heating and the martensite transformation temperature during cooling. The temperature delta is calculated using the difference between A_f and M_s [32]. In applications, low hysteresis is needed for quick actuation control and high hysteresis is needed for maintaining deployment after actuation [32].

Shape change effects can be categorized into three major types: one-way shape memory effect, two-way shape memory effect, and pseudoelasticity or superelasticity.

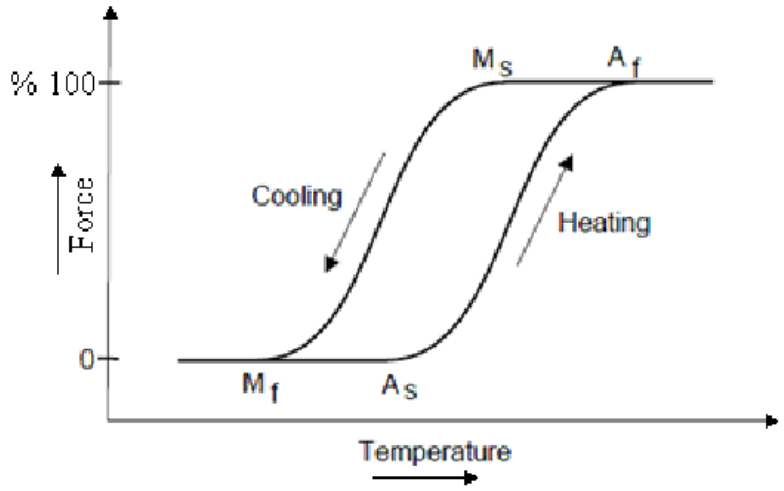

Figure 2-2: SMA hysteresis curve [36].

One-way SMAs are deformable in the martensite phase and return to their trained shape when heated above their transformation temperature. Two-way SMAs have a trained shape at both high and low temperatures, allowing for thermally activated actuation to two distinct and repeatable shapes. Pseudoelasticity is present when the SMA is held above its A_f temperature and reverts to its trained shape without thermal activation [34].

SMA shape setting can be achieved by holding the desired austenitic shape with a mold and heat treating at 400 °C - 550 °C [37]. The annealing temperature is typically held for 5 minutes - 25 minutes. Annealing time impacts critical properties such as hysteresis, A_s, A_f, M_s, M_f, and recovery stress [38]. Quenching immediately after annealing helps set the SMA shape [37].

Nitinol is a favorite among commercially available SMAs due to its ability to recover large amounts of strain and high volumetric work output [39, 40]. Nitinol is a nickel-titanium alloy named for its constituent compounds (NiTi) and its discovery at the Naval Ordnance Laboratory (NOL) [32]. Nitinol properties are compared to other commercially available alloys in Table 2.1. Other common SMAs often include some non-inclusive/non-exclusive combination of nickel, titanium, copper, aluminum, and zinc [40]. The makeup of an SMA affects its mechanical properties such as transformation temperature, deformation recovery, stiffness, and fatigue [41].

Table 2.1: Properties of Common SMAs [42, 43, 44]

Alloy	**Transformation Temperature (°C)**	**Transformation Hysteresis (°C)**	**One-Way Strain (%)**	**Two-Way Strain (%)**
NiTi	-50 - 110	30	8	5
CuZnAl	-180 - 100	20	4	2
CuAlNi	-140 - 100	35	4	2

2.2 Shape Memory Alloy Actuators

SMAs are well-suited for actuators due to their simplicity, high energy and strain capabilities, low shock, and minimal contamination such as fluid or dust [45, 46]. Typical actuators include simple, low SWaP single-use actuators and more complex, high SWaP repeatable actuators.

Single-use SMA actuators are implemented for one-time use cases such as deployment of solar arrays, antennas, booms, trusses, shutter mechanisms, and scientific instruments. Benefits include simplicity and reliability at the expense of repeatable actuation beyond deployment. TiNi Aerospace's Frangibolt, pictured in Figure 2-3, is an example of a 25 gram hold down and release mechanism (HDRM) capable of releasing loads of 2.8 kN. The Frangibolt uses an SMA shell to fracture a bolt at a designated break point when heated [47]. Similarly, Arquimea's REACT is a low-shock COTS HDRM which has a mass of 268 grams and is capable of release loads of 15 kN [48]. Sierra Nevada Corporation's Fast-Acting Shockless Separation Nut (FASSN) is another release mechanism with an SMA trigger which releases a caged flywheel and subsequently releases a bolt. FASSN has a combined mass of 4.9 kg and can release a maximum load of 133.4 kN [49]. The aforementioned HDRMs are shown in Figure 2-3. Comparable HDRMs are evaluated in Table 2.2 according to mass, size, and maximum release load.

The Aerospace Corporation's nitinol SMA latch, developed for daisy-chaining mechanical and electrical connections on the Power Sphere nanosatellite, is an example of a single-use rotary actuator. Depicted in Figure 2-4, the nitinol strip is folded at 180° while stowed and opens to a fixed angle in order to connect the solar arrays in the desired spherical shape [52]. Similarly, Guzik and Benafan developed a single-

Figure 2-3: COTS single-use release mechanisms. Left to right: TiNi Aerospace's Frangibolt, Arquimea's REACT, and Sierra Nevada Corporation's FASSN [47, 48, 49].

Table 2.2: COTS Single-Use Release Mechanisms

Vendor	**Actuator**	**Model**	**Release Load (kN)**	**Mass (g)**	**Size (cm)**
TiNi Aerospace [50]	Mini Frangibolt	FD04 7V	0.7	8	1.1⌀x 1.3
TiNi Aerospace [47]	Frangibolt	FC2	2.8	25	1.6⌀x 2.4
Starsys Research [51]	QWKNUT	3K	13	200	7.6 x 5.1 x 4.1
Arquimea [48]	REACT	15KN V2	15	268	5.6⌀x 4.3
Sierra Nevada Corporation [49]	Fast-Acting Shockless Separation Nut (FASSN)	30K	133	4,900	12.7 x 12.7 x 30.5

use rotary hinge for CubeSat solar panel deployment using a superelastic flat nitinol plate. Figure 2-4 shows the SMAs folded around a hinge pin with a hard stop hinge bracket to limit final actuation angle. After deployment, a latch engages to hold the solar panels to the required angle [53].

Multiple-use SMA actuators allow repeatable deployment on-orbit beyond initial deployment after launch. Repeatable SMA actuators generate usable work using two different mechanisms: contraction in length or reversion to a trained shape. Contraction in length is generally used with wire-based actuators, where the relatively small contraction can be multiplied via coiled SMA springs as shown in Figure 2-5. The change in length can also be turned into linear motion or rotational motion. Examples of such mechanisms are shown in Figure 2-6. When pairing a contraction method with an oppositional return mechanism, continual actuation is required in

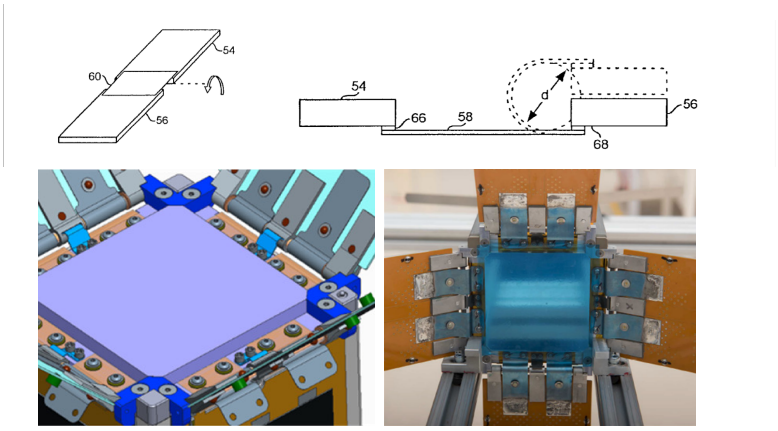

Figure 2-4: Single-use flat SMA rotary actuators for solar panel deployment. Top: The Aerospace Corporation's nitinol SMA latch hinge [52]. Bottom: Guzik and Benafan's SMA deployment mechanism [53].

order to maintain the actuated position. This is demonstrated in the bias springs in Figure 2-5 and Figure 2-6, as well as the flexure mechanism in Figure 2-6. The mini rotary actuator requires continued low power consumption to maintain its actuated position [54].

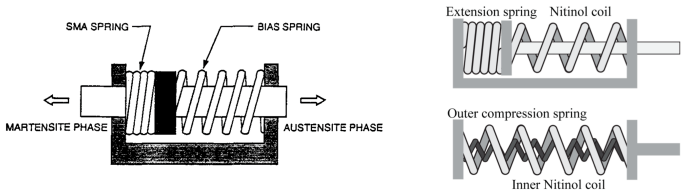

Figure 2-5: Repeatable actuators using SMA springs in opposition to bias springs [55, 56].

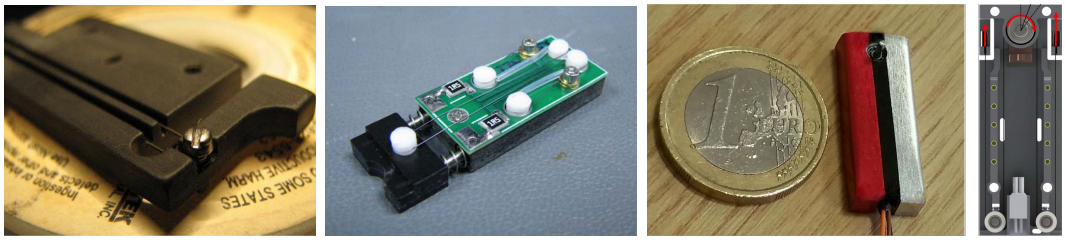

Figure 2-6: Repeatable actuators using flexures and pulleys. Left to right: The Aerospace Corporation's SMA actuator for AeroCube 2 [57], The Aerospace Corporation's SMA actuator for AeroCube 3 [57], size comparison of a coin-sized mini rotary actuator [54], SMA pulley system enabling coin-sized mini rotary actuator [54].

2.3 FLAPS Background and Requirements

The FLAPS concept aims to use two SMA actuators in a bending architecture to provide multiple-use, controllable actuation. The original inspiration was to develop a small, lightweight hinge to repeatably actuate a solar panel for differential drag control. Thus, the original range requirement was to actuate to multiple angles between 0° (stowed) and 180° (fully deployed) [38]. Figure 2-7 shows a 3U CubeSat with four deployable solar panels deployed to 90°.

Figure 2-7: 3U CubeSat with deployable solar panels. Figure generated by Christian Haughwout [58].

A secondary application for the FLAPS hinge was to repeatably actuate a calibration target for an Earth-imaging CubeSat, shown in Figure 2-8. The hinge would sit in a similar position as the solar panel architecture and the target would begin stowed at an angle of 0°. Once deployed, the calibration target would rotate in and out of the field of view (FOV) of the thermal imaging cameras. This would require repeatable actuation between the angles of 90° and 180°.

The SMA hinge bending architecture was selected over contraction in length due to the larger potential shape change with minimal complexity. While contraction can be combined reliably with mechanisms such as springs and pulleys to increase throw, these components add complexity to an already SWaP-constrained solution. The FLAPS hinge uses two one-way nitinol actuators annealed in a bending architecture and mounted to actuate in opposing directions, shown in Figure 2-9. The first SMA is

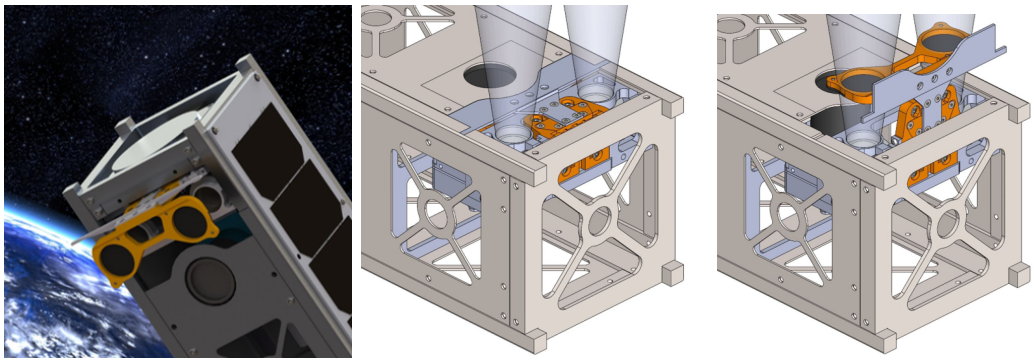

Figure 2-8: FLAPS as an actuation method for calibration targets. Left: BeaverCube with deployable calibration target shown in orange. Center: BeaverCube with stowed calibration target at an angle of 0°. Right: BeaverCube with deployed calibration target at an angle of 90°. Figures generated by Paula do Vale Pereira and William Kammerer [59].

meant to actuate the hinge +90° from the unactuated position and the second SMA is meant to actuate the hinge -90° from the unactuated position. The hinge is actuated by running power through one SMA at a time to heat it above its A_s temperature. A pair of one-way nitinol actuators was selected for prototype development due to the ease of training methods and the implementation of closed-loop control. A single two-way nitinol actuator would have required more precise thermal characterization and control of the SMA, as well as more complex annealing processes [32].

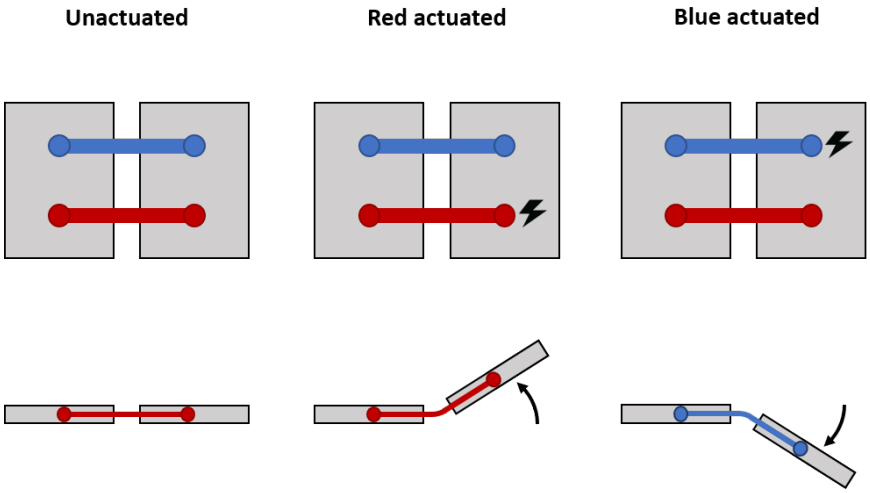

Figure 2-9: Rotary hinge concept with two opposing one-way SMA actuators shown in blue and red. Active Joule heating indicated by lightning bolt [60].

Nitinol was selected for its high volumetric work output, recoverable strain, trans-

formation temperature range, and availability. Relevant nitinol properties are shown in Table 2.3. While a deployed CubeSat solar panel can expect to experience temperatures upwards of 140 °C, an 80 °C transformation temperature was determined to be adequate for prototype functionality testing [38].

Table 2.3: Properties of Nitinol [42, 43, 44, 39]

Property	**Value**
Density, ρ ($\frac{\text{kg}}{\text{m}^3}$)	6450
Martensite Young's Modulus, E (GPa)	28 - 41
Austenite Young's Modulus, E (GPa)	75 - 83
Transformation Temperature Range (°C)	-50 - 110
One-Way Recoverable Strain, ε (%)	8
Two-Way Recoverable Strain, ε (%)	5
Work per Volume ($\frac{\text{J}}{\text{cm}^3}$)	10
Martensite electrical resistivity ($\Omega\ \mu m$)	0.76
Austenite electrical resistivity ($\Omega\ \mu m$)	0.82

2.4 FLAPS Force Derivations

Given the pair of one-way SMAs, the actuation force exerted by the actuated SMA must overcome the bending resistance of the opposing SMA. The actuation force of the actuated SMA is derived from its strain during deflection as characterized by Young's modulus. Actuation force can be calculated using:

$$F_{actuation} = AE\frac{\Delta L}{L_0}\sin\alpha \tag{2.1}$$

where A is the cross-sectional area of the actuator in inches squared, E is Young's Modulus in pounds per square inch, ΔL is the change in length in inches, L_0 is the original length of the actuator in inches, and α is the difference between the actuator angle and the encoder measurement angle in degrees [60, 61]. The cross-sectional area of the actuator, regardless of geometry, will affect the actuation force supplied to the hinge. The full derivation is explained in Appendix A.

The bending resistance from the opposing SMA can be approximated at small

angles as a cantilever beam with a force exerted at a design-defined distance. Bending resistance can be calculated using:

$$F_{resistance} = \frac{3EI\delta}{{L_0}^3} \tag{2.2}$$

where E is Young's Modulus in pounds per square inch, I is the cross-sectional second moment of area in inches^4, δ is the deflection in inches, and L_0 is the original length of the actuator in inches [60, 61]. The geometry of the actuator will affect resistance force, as indicated by the cross-sectional second moment of area term. Thus, the cross-sectional geometry can be tuned to a provide low resistance force.

In the following chapters, the progression of two different FLAPS hinge designs will be tracked: a rectangular cross-sectional actuator and a circular cross-sectional actuator. The different cross-sectional geometries provide different resistance forces, while comparable cross-sectional areas are maintained to provide similar actuation forces. Key differences are outlined in Table 2.4. Mechanical constraining methods are tailored to the specific manufacturing and architecture limitations of each actuator type.

Table 2.4: Two Approaches to the FLAPS Hinge

Property	**Flat Hinge**	**Round Hinge**
Actuator Cross-Section Geometry	Rectangle	Circle
Actuator Cross-Section Dimensions (mm)	2 x 0.25	⌀0.5
Actuator Cross-Section Area (mm^2)	0.5	∼0.4
Mounting Method	Bolt holes mounted on both ends	Ring terminals mounted only on stowed end
Mechanical Structure	Supported hinge	Supported hinge

2.5 FLAPS Electronics and Controls

Repeatable precision pointing is enabled by active control of the hinge. To actuate the hinge back and forth, Joule heating was applied by alternately running current

through each SMA. Power to the actuator was routed via a 1U PCB and controlled with an Arduino Uno. A non-contact, magnetic, rotary encoder was mounted to the hinge in order to measure hinge angle and enable feedback control. The control design and selected electronics were driven in part by the requirements of a zero gravity flight which was flown in July of 2019.

As shown in the full electronics block diagram in Figure 2-10, the PCB can supply power from a 28 V wall plug to the microcontroller unit (MCU), magnetic encoder, accelerometer, analog-to-digital converter (ADC), and instrumentation amplifier. The MCU is an Arduino Uno that provides real-time control of the hinge. The accelerometer was included for the zero gravity flight in order to determine when the plane was experiencing sufficient microgravity prior to actuating the hinge. Voltage to the SMA was pulse width modulated (PWM) with a set voltage and varying duty cycle through a MOSFET. Duty cycling is preferred when electrically actuating SMAs to avoid overheating the thermally-sensitive alloy [57]. Current across the SMA was calculated using a current shunt of known resistance in series with each SMA. Average voltage was calculated using the measured voltage across each SMA and the duty cycle. Due to the relatively low resistance of the SMAs, the added resistance of all wires are included in these calculations [62].

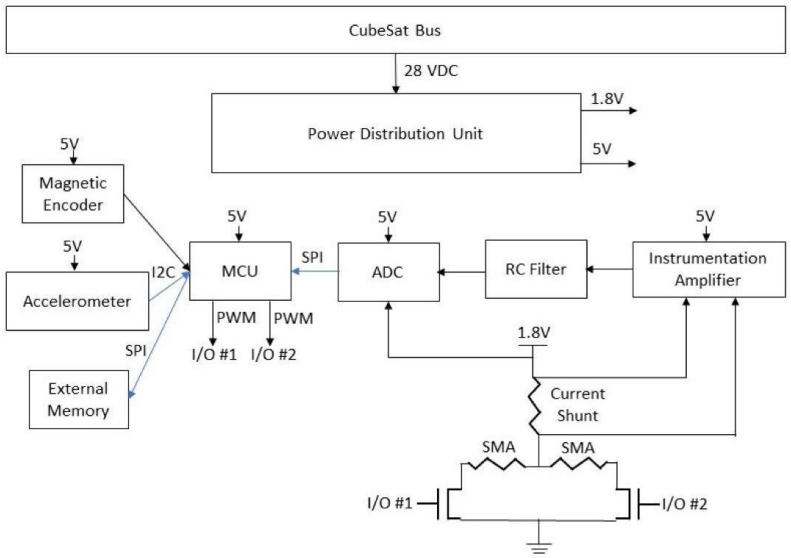

Figure 2-10: Full electronics schematic. Figure generated by Charles Lindsay [62].

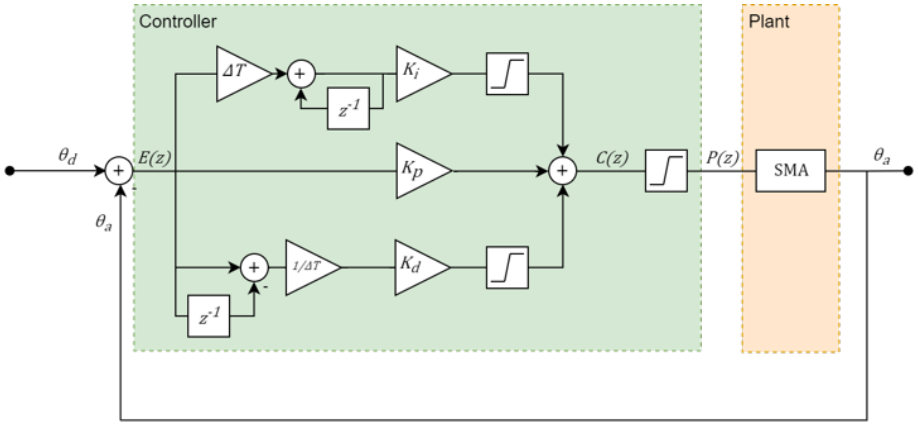

Figure 2-11: Full controls schematic. Figure generated by Shreeyam Kacker [66].

A simple control loop was implemented due to the generally linear, time-invariant (LTI) transfer function of low-powered SMAs [62, 63, 64]. A proportional-integral-derivative (PID) controller was found to work well with the system, shown in Figure 2-11. The primary drivers for the controller were to minimize overshoot and enable a quick response time. Overshoot was minimized because the one-way SMA inherently cannot return to a previous position without actuation of the opposing SMA [62]. A quick response time was needed to actuate within the 17 seconds of microgravity per parabola on the zero gravity flight [65].

The plant was characterized by using step response data for each of the two FLAPS hinge designs. The hinge angle was recorded for multiple different duty cycles until it reached its saturation angle, then the step response data was averaged for each duty cycle and passed through MATLAB's robust response time algorithm to determine the transfer function. The controller gains were also tuned using the robust response time algorithm. All data analysis was performed in MATLAB [62].

Chapter 3

Flat Hinge Development

The flat hinge combines two one-way SMA actuators in an antagonistic bending architecture.[1] The actuators are supported by a traditional hinge structure to prevent torsion [67]. The rectangular cross-section of the actuator was tuned to maintain actuation force and minimize resistance force. Joule heating is used to actuate the SMAs using closed loop control.

3.1 Previous Work

Previous work by Maxim Khatsenko demonstrated the actuation of two free-standing, antagonistic, one-way SMA actuators with rectangular cross-sections. The Khatsenko hinge actuated over a total range of 90°. The actuators were fabricated from 0.1 mm thick nitinol plate stock with a transformation temperature of approximately 50 °C. The actuators were annealed at 420 °C and mounted in opposing directions in order to achieve repeatable, multi-use actuation. Amperages of 1 A - 6 A were used to actuate a truncated solar panel against additional gravity loading [38]. The Khatsenko hinge

[1]This iteration of the FLAPS flat hinge was developed by a team of graduate and undergraduate students in the Space Telecommunications, Astronomy, and Radiation (STAR) Lab. The mechanical subteam consisted of the author, graduate student Paula do Vale Pereira, and undergraduate student Mario Contreras. The electrical subteam consisted of undergraduate students Charles Lindsay, Mario Contreras, Shreeyam Kacker, Ethan Sit, Raymond Huffman, and Raul Largaespada. The controls subteam consisted of undergraduate students Mario Contreras and Shreeyam Kacker. The test subteam consisted of undergraduate students Joseph Ward and Ronak Roy. Graduate student Christian Haughwout supported the project in an advisory role.

concept is shown in Figure 3-1 and the hinge prototype is shown in Figure 3-2.

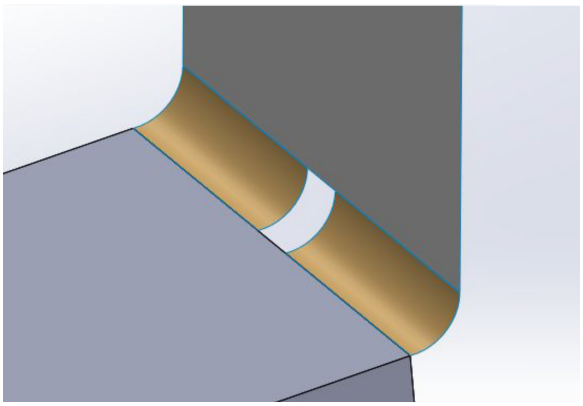

Figure 3-1: Free-standing FLAPS hinge concept. Figure generated by Maxim Khatsenko [68].

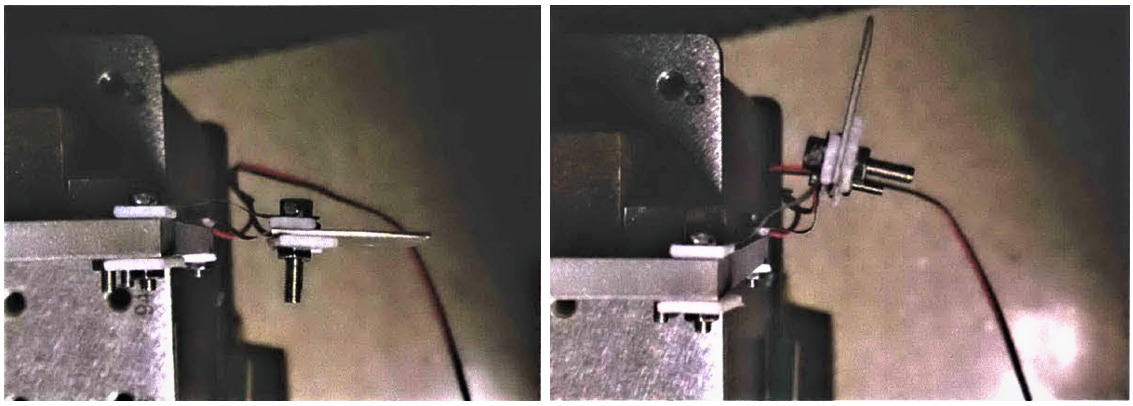

Figure 3-2: Free-standing FLAPS hinge prototype. Figure generated by Maxim Khatsenko [38].

3.2 Flat Hinge SMA Actuator

The primary function of the SMA actuator is to bend with enough force against the opposing SMA actuator and the attached deployable. SMA actuator shape was driven by actuation force, bending resistance, and manufacturability. Actuation force is generalized with respect to cross-sectional area, giving a specific equation for a rectangular cross-section as follows:

$$F_{actuation} = bhE\frac{\Delta L}{L_0}\sin\alpha \tag{3.1}$$

where b is the cross-sectional base of the actuator in inches, h is the cross-sectional height of the actuator in inches, E is Young's modulus in pounds per square inch, ΔL is the change in length in inches, L_0 is the original length of the actuator in inches, and α is the difference between the actuator angle and the encoder measurement angle in degrees [61].

The rectangular cross-sectional geometry of the actuator is represented by the second moment of area, given by the following equation:

$$I_{rectangle} = \frac{bh^3}{12} \tag{3.2}$$

where b is the cross-sectional base of the actuator in inches and h is the cross-sectional height of the actuator in inches.

Resistance force is generalized with respect to the second moment of area, combining Equation 2.2 and Equation 3.2 to yield the following for the rectangular cross-sectional actuator:

$$F_{resistance} = \frac{Ebh^3\delta}{4{L_0}^3} \tag{3.3}$$

where E is Young's modulus in pounds per square inch, b is the cross-sectional base of the actuator in inches, h is the cross-sectional height of the actuator in inches, δ is the deflection in inches, and L_0 is the original length of the actuator in inches.

Actuation force is proportional to the cross-sectional height, while bending resistance is proportional to the cube of the cross-sectional height. Thus, the cross-sectional height can be optimized for net force exerted. The rectangular cross-section was further leveraged by using the cross-section's directionality to the advantage of the single axis of rotation. A larger width would make bending around the other two axes of rotation more difficult, as well as prevent unwanted torsion of the hinge. Since the cross-sectional base is directly proportional to both forces, the cross-sectional base can be considered independent of net force exerted.

3.2.1 SMA Actuator Design

Multiple different thicknesses of nitinol plates were evaluated when considering actuator height: 0.15 mm, 0.25 mm, and 0.5 mm. The 0.25 mm thick nitinol plate performed the best in terms of exerting an adequate actuation force to actuate against its own bending resistance. Thus, height was minimized to 0.25 mm and width was held at 2 mm.

The effective length of the actuator is much longer in comparison, 50 mm, in order to increase the moment arm of the hinge. The effective length is measured between the connection points of the electronics, since that is the heated portion of the SMA.

The connection method between the SMA and the electronics was also a concern due to the quick oxidation of the material. Soldering would require removing the oxidation layer with flux. Soldering would also couple the mechanical and electrical connection points into a single point of failure. Set screws could prove unreliable during actuation due to the movement of the SMA actuator within the hinge. A bolting approach was eventually selected, since the oxidation layer could be reduced on the connection points via some light sanding. By mounting the SMA immediately after sanding, the formation of the oxide layer could be mitigated between the electrical contacts.

The bolting approach required a larger area for electrical connection points on either end of the actuator and a hole through the center of the larger area [60]. The final shape is shown in Figure 3-3.

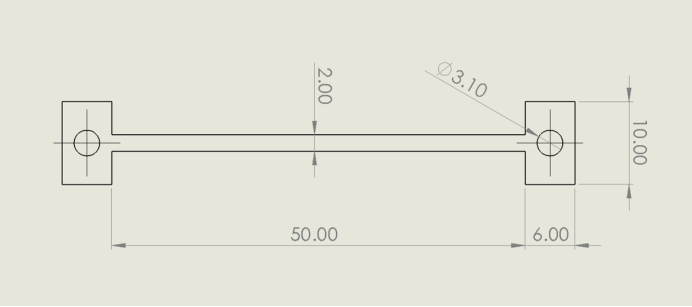

Figure 3-3: Drawing of SMA actuator shape (in mm) [60].

3.2.2 SMA Actuator Manufacturing

In order to manufacture the SMA actuator, 0.25 mm thick nitinol plate was sourced from Kellogg's Research Labs [69]. The highest transformation temperature was selected to avoid any superelastic effects and prevent accidental actuation in the intended test environment. Thus, nitinol with a transformation temperature of 80 °C was chosen. While a deployed CubeSat solar panel can expect to experience temperatures upwards of 140 ° C, the 80 °C transformation temperature was adequate for prototype functionality testing [38].

The actuator was precision waterjetted on an OMAX MicroMAX in order to preserve the material's shape memory effect. The OMAX MicroMAX has a linear positional accuracy of 0.00254 mm [70]. The stock was mounted to an aluminum plate with multiple layers of aluminum tape in order to keep the thin material in place. The waterjetting method and finished actuators are shown in Figure 3-4.

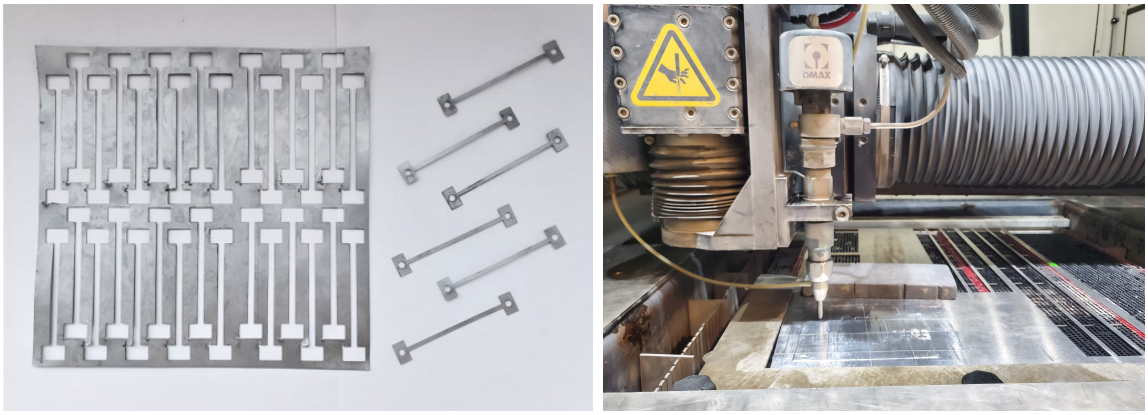

Figure 3-4: SMA actuator waterjetting. Left: SMA actuators waterjetted out of 0.25 mm thick nitinol stock. Right: Mounted nitinol stock fixed inside MicroMAX waterjet.

3.2.3 SMA Actuator Annealing

The waterjetted actuators were trained to the appropriate shape by being placed in a mold, annealed in an annealing oven courtesy of the MIT Glass Lab, and quickly quenched in cool water. Critical parameters were annealing temperature, annealing time, and annealing angle. The annealing temperature was set at 500 °C, which falls

within the range of acceptable nitinol annealing temperatures of 450 °C - 550 °C [71]. Different annealing angles and time lengths were evaluated.

In order to evaluate different annealing angles, aluminum molds were machined with inset channels to hold the actuator to the desired shape. Four different annealing angles were considered as shown in Figure 3-5: 90°, 120°, 160°, and 180°. The angle is measured about the center of the actuator with the as-waterjetted shape measuring an angle of 0°. Since the annealed angle is not the final actuation angle, the SMAs were overtrained to provide the largest final angle possible. The original 180° hinge range required an individual range of 90° from either SMA actuator. Thus, the 180° mold base was selected for prototype annealing.

The minimum allowable radius of curvature was also taken into account when machining the molds. In order to remain within the elastic deformation range, the minimum radius of curvature is approximately 10 times the thickness of the nitinol [69]. Accordingly, the 0.25 mm thick plate could be annealed to a minimum bending radius of 2.5 mm.

The SMA actuators were fastened in place with an aluminum lid and bolts. Slots were added to the lids in varying numbers in order to test different quenching speeds, also seen in Figure 3-5. Lids with more slots quench faster than those with fewer slots. The quenching speed helps set the trained shape for the SMA. Thus, the four slot lids (not pictured) yielded the best actuator performance after annealing and quenching.

Annealing times of 5 minutes - 30 minutes were tested for the SMA actuators. The annealing time had to be sufficient to heat both the mold and the actuator up to the annealing temperature, then hold the assembly at that temperature for an adequate amount of time. It was also important to avoid overannealing, which would make the SMA very brittle. The actuators performed best in terms of trained actuation angle when annealed for 25 minutes.

Overall, critical annealing parameters included an overtrained angle of 180°, a lid with four slots to promote faster quenching, and an annealing time of 25 minutes.

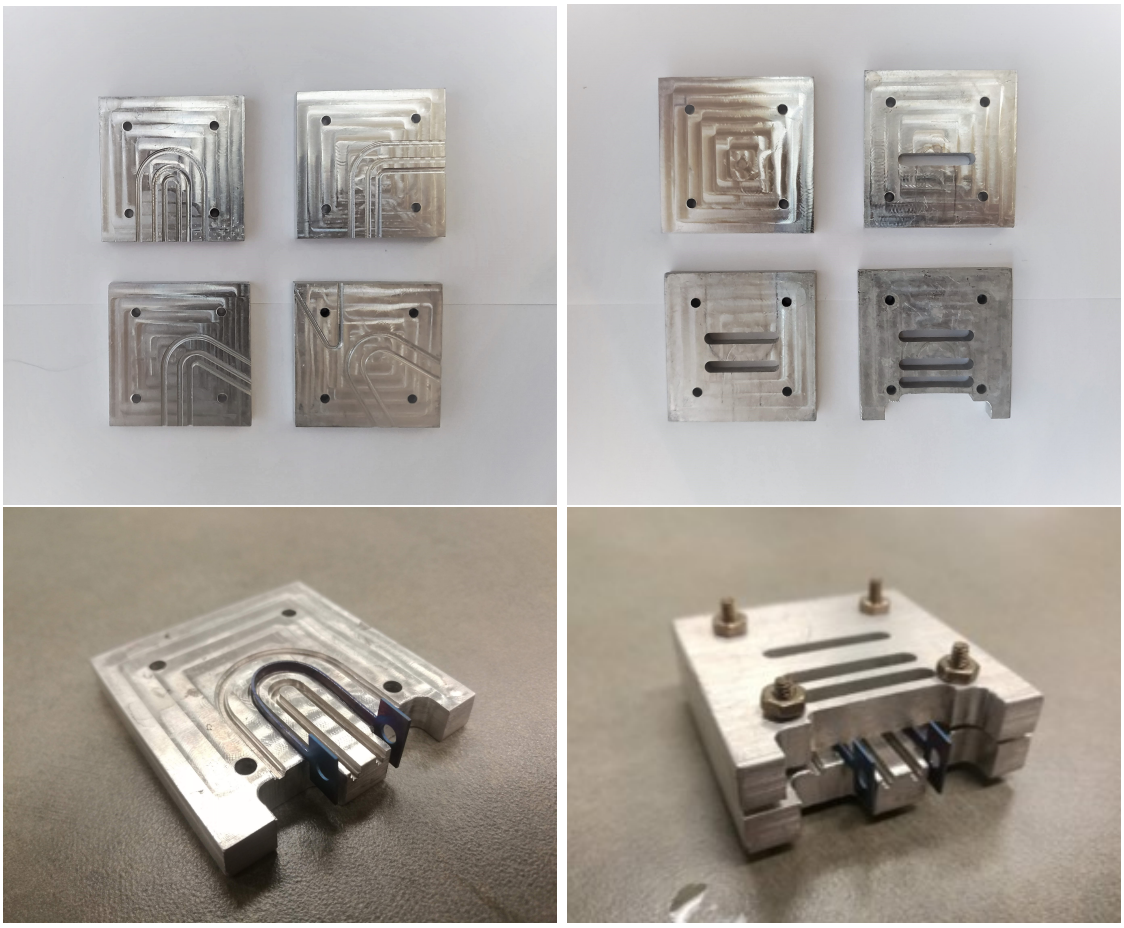

Figure 3-5: Annealing molds. Clockwise from top left: Mold bases, mold lids, assembled mold with actuator, mold base with inset actuator at 180° turn.

3.3 Flat Hinge Prototyping

Primary concerns during prototyping of the hinge were proper constraint of the SMAs, electronics integration, and heat tolerance.

Due to demonstrated torsion on the Khatsenko hinge, a supporting structure was included to constrain the SMAs to bend around a single axis [38]. An open cavity was left in the center of the hinge to bend the actuators along the hinge's neutral axis. Placing both SMAs along the neutral axis minimized strain as one SMA actuated against the other. Supporting pins and bushings were placed on either side of the pair of SMA actuators to provide additional support. The support pins also prescribed a single axis of rotation for both actuators. Recessed slots matching the shape of the actuators were included to place actuators at the neutral axis. The SMAs were

mounted in place with bolts and nuts inside the recessed slots. The full mechanical hinge assembly is displayed in Figure 3-6.

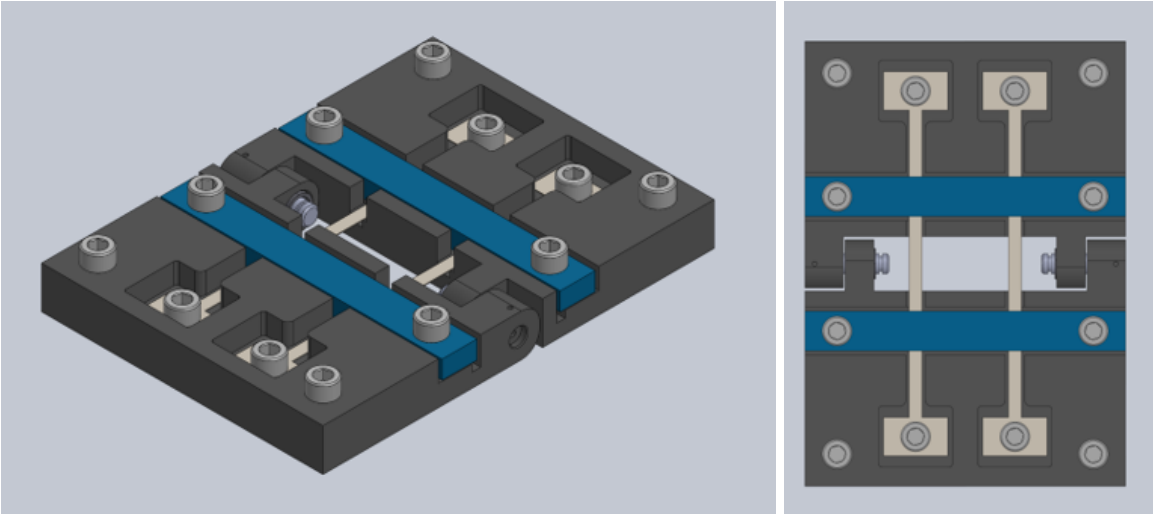

Figure 3-6: Isometric and top views of the flat hinge design [67].

3.3.1 Flat Hinge Assembly

The hinges were 3D printed out of Onyx on a Markforged printer for quick prototype development. Onyx is a carbon-reinforced plastic composite with a plastic matrix heat deflection temperature of 145 °C and a carbon fiber reinforcement heat deflection temperature of 105 °C [72]. This is above the SMA transformation temperature of 80 °C, lowering the chance of the nitinol melting into the hinge itself. While the SMAs did reach temperatures to melt the surface of the hinge, the overall structural integrity of the hinge was unaffected.

The two halves of the hinge are identical for easy fabrication and assembly, with a metal pin and a bushing press fit into each side. The SMAs were installed by lightly sanding the connection points, placing within the recessed slots, and fastening in place with a bolt and nut. The entire hinge assembly has mounting holes to affix one side to a mockup CubeSat cap and the other side to a mockup deployable panel.

On the CubeSat cap side of the hinge, the leads were attached via ring terminals to the bolts at the SMA connection points. On the deployable side, both SMA connection points were connected with a copper plate. The single connection point

was implemented because only one SMA needed to be actuated at a time. A single wire was routed back to the PCB to minimize the number of external floating wires.

During preliminary testing, the trained SMAs were bending away from the recessed slot during actuation. This caused the Joule heating to be ineffective in actuating the hinge, since the actuator was already in its trained shape and would not exert any additional force on the hinge around the axis of rotation. Buckling straps, shown in blue in Figure 3-6, were added to keep the SMA actuators within their recessed slots. The buckling straps were bolted onto the hinge after installation of the SMA actuators.

The encoder's magnetic actuator was press fit into the side of the hinge on the axis of rotation. The encoder body was aligned with the actuator using a 3D printed mount that fastened to the mockup CubeSat cap. The full hinge prototype is displayed in Figure 3-7.

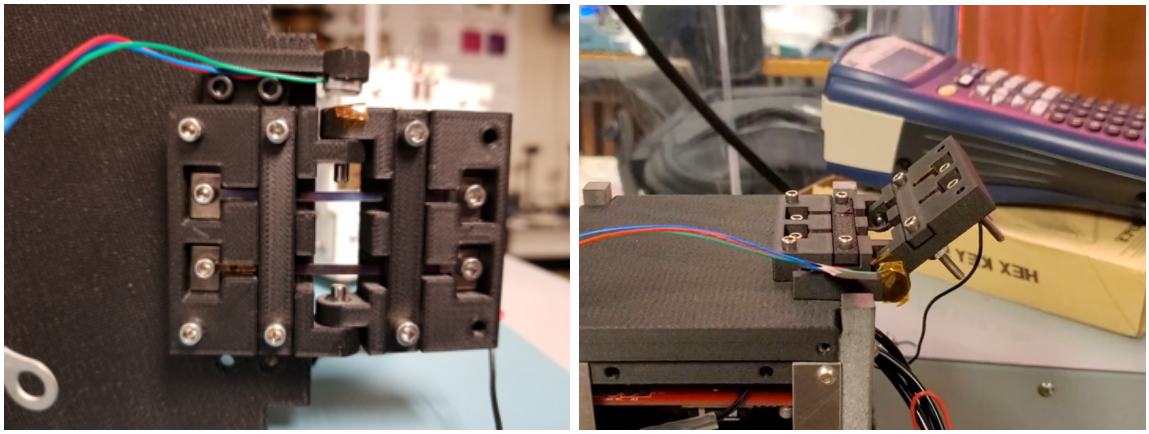

Figure 3-7: Full flat hinge prototype [67].

3.4 Flat Hinge Controls

In order to implement closed loop control, the hinge was characterized and the gains were tuned. The plant transfer function was determined using a step response approach where actuation angle for 5 different duty cycles (DC) were measured: 12 DC, 14 DC, 16 DC, 20 DC, and 40 DC. Measured angle and power data was filtered using a 200 sample moving-average filter, shown for a single trial in Figure 3-8 [62]. Power

was averaged in order to determine the average input power for each duty cycle: 0.095 W for 12 DC, 0.130 W for 14 DC, 0.140 W for 16 DC, 0.230 W for 20 DC, and 1.050 W for 40 DC.

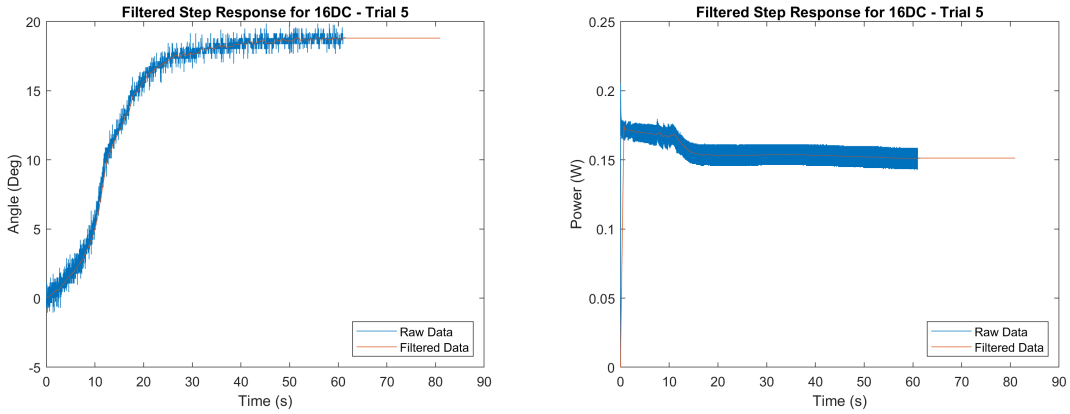

Figure 3-8: Filtered step responses for a single 16 DC run. Data and script generated by Mario Contreras [62].

Each duty cycle was then averaged, artificially elongated to reach steady state, and recorded in Figure 3-9. Outliers were excluded due to limited actuation range, likely caused by the buckling of the SMAs. The plant transfer function was approximated with a pure 2nd order system with two poles. The addition of pole-zero pairs were investigated in order to account for the time lag from heating the SMA to the initial A_s prior to actuation [62].

Figure 3-10 shows the three system models that were evaluated: a 2nd order system, a 2nd order system with 1 additional lag, and a 2nd order system with 2 additional lags. Since the additional lags yielded limited improvement, the original 2nd order system with 2 poles was ultimately selected for simplicity and speed. The final transfer function is described by Equation 3.4:

$$\theta(s) = \frac{1.144}{s^2 + 0.183s + 0.01597} \tag{3.4}$$

Initial controller gains were tuned around the low power operating condition of 16 DC, or 0.14 W, using the step response data. Initial tuning was performed with MATLAB's robust response time algorithm followed by additional root locus tuning.

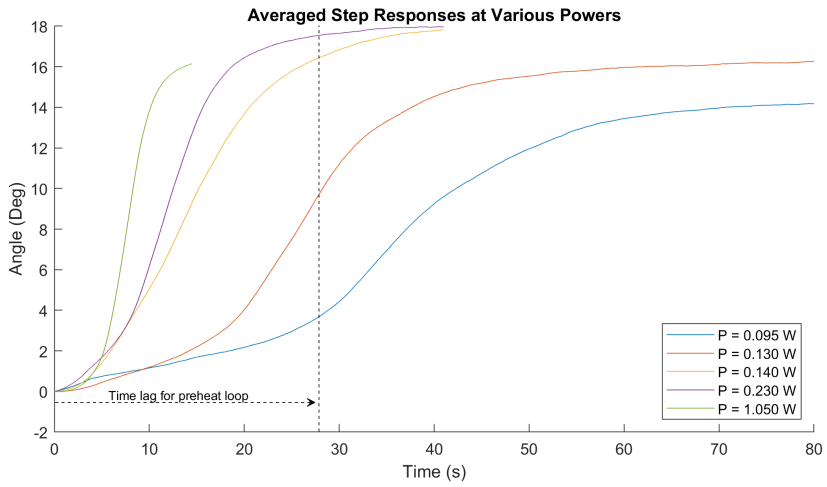

Figure 3-9: Step response output angle with respect to different power levels. Figure generated by Charles Lindsay [62].

This gave the following set of gains: $K_p = 0.04379$, $K_i = 0.002789$, and $K_d = 0.1442$ [62]. The step response for the closed loop system in shown in Figure 3-11. The flat hinge response has a simulated rise time of approximately 4 seconds, a settling time of approximately 15 seconds, and an overshoot of approximately 8%.

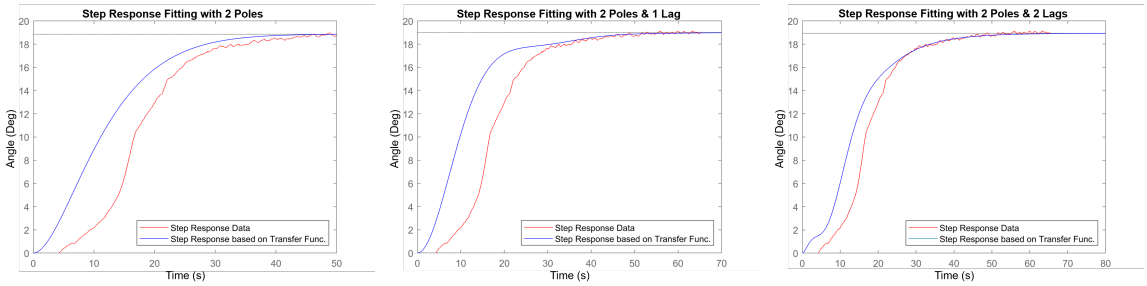

Figure 3-10: Comparison of step response fitting models for 16DC - Trial 5 data. Figure generated by Mario Contreras [62].

When implemented, the output power was much lower than expected due to an issue with the Arduino duty cycle and power output. In order to adjust for zero gravity flight time limitations, gain multipliers of 10 and 50 were evaluated. The multiplication factor of 10 returned the following gains: $K_{p,10} = 0.4379$, $K_{i,10} = 0.02789$, and $K_{d,10} = 1.442$. The multiplication factor of 50 returned the following gains: $K_{p,50} = 2.1895$, $K_{i,50} = 0.13945$, and $K_{d,50} = 7.21$ [62].

The SMAs were preheated during testing to minimize excessive overshoot. Exces-

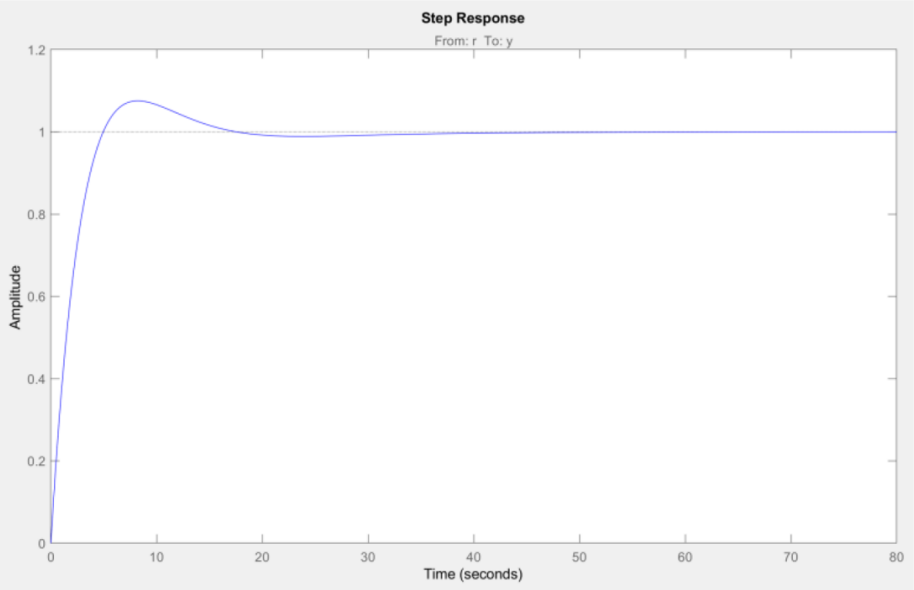

Figure 3-11: Closed loop step response for flat hinge. Data and script generated by Mario Contreras [62].

sive overshoot was caused by a high average power quickly heating the SMA through the transformation temperature [62]. Both increased sets of gains were evaluated to a setpoint of -20°, displayed in Figure 3-12. The factor of 10 gains yielded an overshoot angle of less than 2° over an actuation time of 75 seconds. The factor of 50 gains yielded an overshoot angle of less than 3° over an actuation time of 15 seconds. This was adequate for microgravity testing and the factor of 50 gains were implemented for the zero gravity flight [62].

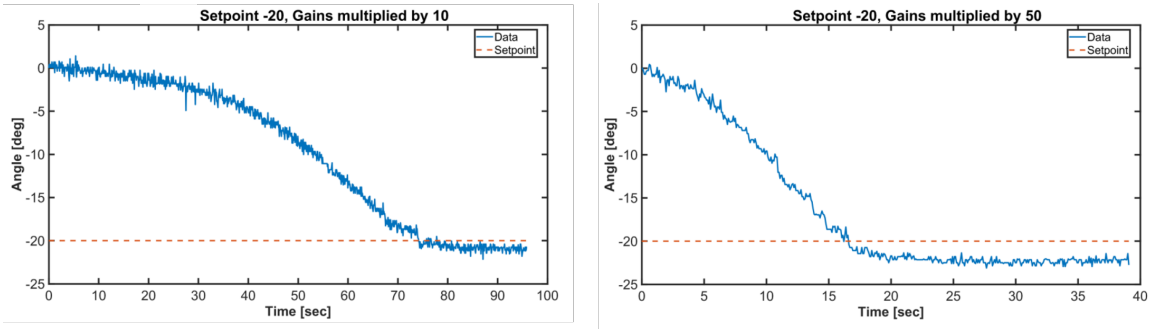

Figure 3-12: Hinge actuation angle with respect to time for a setpoint of -20° and increased gains. Figure generated by Mario Contreras [62].

3.5 Flat Hinge Limitations

The primary limitation of the flat hinge design is the buckling of the SMAs. The length of the actuator, while beneficial for creating a larger moment arm to generate actuation force, creates initial buckling when it separates from the hinge. When the actuator begins slightly bent, it has less actuation force to actuate the hinge. The opposing SMA is also slightly bent in its opposing trained position, creating the same problem in the opposite direction and doubling the loss in actuation range. This effect is demonstrated by Figure 3-13, where each SMA is curved towards its annealed position. During actuation, the non-driven SMA buckles in its annealed direction to further limit hinge range.

Figure 3-13: Buckling in each SMAs annealed direction.

The SMA also buckles due to the fixed connection points. Upon further inspection, the length along the neutral axis changes when actuating from 0° to 90°. When placed along the neutral axis, the SMA is theoretically required to turn at a sharp 90° angle in order to maintain its length and fastened connection points. Since the SMA maintains its trained radius of curvature, the actuator must buckle in order to accommodate the fixed connection points.

Performance degradation was observed in the SMAs as actuation range decreased over time. While the SMA actuators maintained SME through the initial hinge development and controls implementation process, they were occasionally reannealed via Joule heating over the course of several months. This loss in actuation range might

be attributed to the annealing method, annealing parameters, or continual thermal cycling when in use. Over the project lifespan of two years, through hundreds of cycles, the controllable actuation range remained constant at approximately $\pm 20^{\circ}$.

Chapter 4

Round Hinge Development

The round hinge design aims to address the buckling issue caused by fixed connection points on either side of the flat hinge. The round hinge maintains a bending architecture, but mounts both connection points on a single side of the hinge. The SMA loops through the deployable portion of the hinge which allows the SMA to slide through the hinge while maintaining fixed electrical connections. Joule heating is used to actuate the individual SMAs within the hinge structure.

4.1 Previous Work

Previous work by Christian Haughwout used nitinol wire with a circular cross-section to actuate a supported hinge structure through a range of 180°. This actuation range was achieved by overshooting the transformation temperature of 80 °C and using momentum to reach full deployment. The length of the round SMA actuator was approximately 10 mm and fixed at either end using a set screw. The diameter of the SMA wire was 0.5 mm. The SMAs were annealed using Joule heating at a high wattage. The CubeSat cap and deployable solar panel were both PCBs, allowing the electronics of the hinge to be directly routed via traces instead of wires. The SMAs were electrically connected to the PCBs using a copper insert with a slot to slide over the PCB and a hole to insert the wire. The hinge concept is shown in Figure 4-1 and the hinge prototype is shown in Figure 4-2.

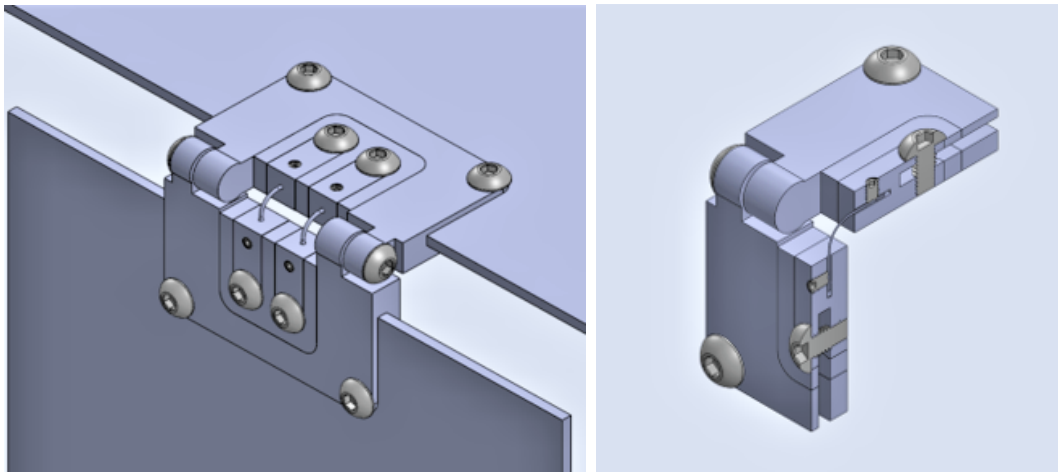

Figure 4-1: Previous FLAPS hinge design with round wire SMA actuators developed by Christian Haughwout [58, 66].

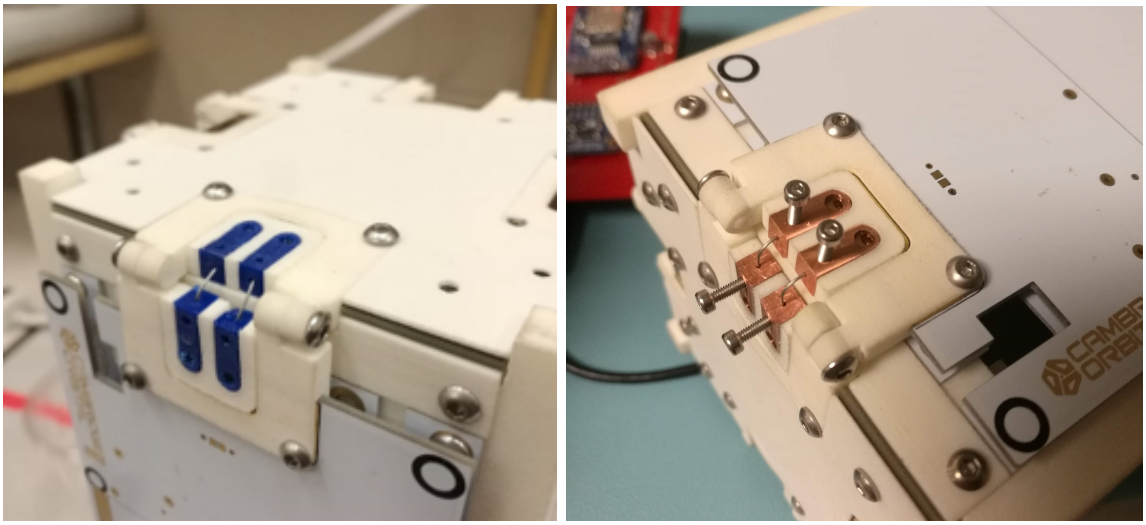

Figure 4-2: Previous FLAPS hinge prototype with round wire SMA actuators developed by Christian Haughwout. Left: CubeSat mock-up with 3D printed inserts. Right: CubeSat mock-up with machined copper inserts [58, 66].

4.2 Round Hinge SMA Actuator

The use of round SMA wires with circular cross-sections contributes to the accessibility of the hinge material and its manufacturing methods. This is due to the availability and low cost of nitinol wire, as well as the ease in switching out waterjetting for a pair of wire cutters. However, the round nitinol wire lacks the directionality of the rectangular nitinol strip, demonstrated by the second moment of area for the circular cross-section:

$$I_{circle} = \frac{\pi r^4}{4} \tag{4.1}$$

where r is the cross-sectional radius of the actuator in inches.

The actuation force from the actuated SMA can be calculated with Equation 4.2:

$$F_{actuation} = \pi r^2 E \frac{\Delta L}{L_0} \sin \alpha \tag{4.2}$$

where r is the radius of the cross-sectional circle in inches, E is Young's modulus in pounds per square inch, ΔL is the change in length of the actuator in inches, L_0 is the original length of the actuator in inches, and α is the difference between the actuator angle and the encoder measurement angle in degrees [61]. Since the actuation force is only dependent on cross-sectional area, regardless of geometry, the same actuation force as the flat hinge can be attained by changing the wire's radius. For the loop architecture in Figure 4-5, $F_{actuation}$ is multiplied by two because the wire doubles back through the actuation region of the hinge. Thus, each individual SMA will effectively contribute twice the cross-sectional area, which is directly proportional to actuation force.

Similar to the rectangular cross-section actuators, the bending resistance is approximated by assuming the wire is a cantilever fixed at one end. The resistance force is dependent on the second moment of area, combining Equation 2.2 and Equation 4.1 to yield the following for the circular cross-sectional actuator:

$$F_{resistance} = \frac{3E\pi r^4 \delta}{4{L_0}^3} \tag{4.3}$$

where E is Young's modulus in pounds per square inch, r is the cross-sectional radius of the actuator in inches, δ is the deflection in inches, and L_0 is the original length of the actuator in inches. The $F_{resistance}$ is also doubled because each actuator has two wires bending in opposition to the actuation force.

4.2.1 SMA Actuator Design

The buckling issue caused by having fixed connections on both sides of the hinge was addressed by moving all fixed connections to a single side. The SMA was looped through the deployed hinge side and routed back to the mounted hinge side. Figure 4-3 shows the SMA actuator with the looped shape, where the free ends of the wire are the connection points. The round wire is well-suited for this double-back architecture because it can be easily bent into different shapes with minimal additional friction. There is also no change to the second moment of area based on orientation. The radius of curvature of the loop is irrelevant to the actuation of the hinge, since the shape memory effect is not being used in that direction. While the circular cross-sectional shape means a smaller actuation force to bending resistance ratio, the concept is still viable when compared with the previous flat hinge design.

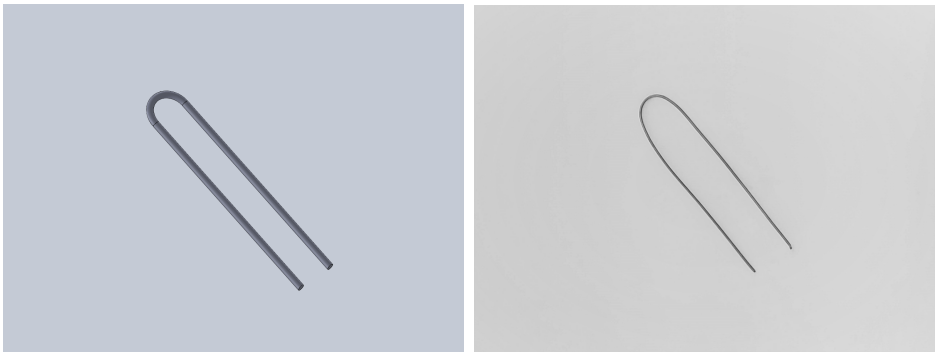

Figure 4-3: Loop concept with 0.5 mm diameter SMA wire.

Multiple round wire diameters were sourced from Kellogg's Research Labs and evaluated: 0.25 mm, 0.5 mm, and 1 mm. The actuation force provided by each wire is directly proportional to the cross-sectional area, giving preference to the larger diameter wires. While the 1 mm wire could provide a larger actuation force, the actuation force made it difficult to actuate against itself. The 0.25 mm wire was adequate but provided significantly less actuation force due to the proportionality between force and the square of the radius. When doubled to accommodate for the looped shape, the 0.5 mm wire had a cross-sectional area and thus actuation force comparable to the flat hinge actuator. Thus, the 0.5 mm wire was selected

for prototyping. The transformation temperature of 80 °C was maintained due to availability, cost, and adequacy for prototyping purposes. Wire cutters were sufficient for cutting nitinol wire to the correct length.

The round wires were annealed using resistive heating supplied by an electrical power source. This was due to limited access to the annealing ovens. The wire was cut to the required length and mounted into a previous iteration of the round hinge to maintain the correct shape. The two halves of the hinge were taped together to simulate the correct radius of curvature at a bending angle of 180°. The wires were overtrained in order to maximize actuation angle.

Leads were attached to either end of the actuator and 7 A of current was passed through the wire until it just began to glow red. Nitinol begins to glow red at 600 °C, which ensures that it reaches the critical annealing temperature of 500 °C [69]. The power source was then turned off, the leads were removed, and the SMA was quenched to room temperature. After removal from the mold, the 80 °C transformation temperature actuator was dipped into 100 °C boiling water to confirm the shape setting was effective.

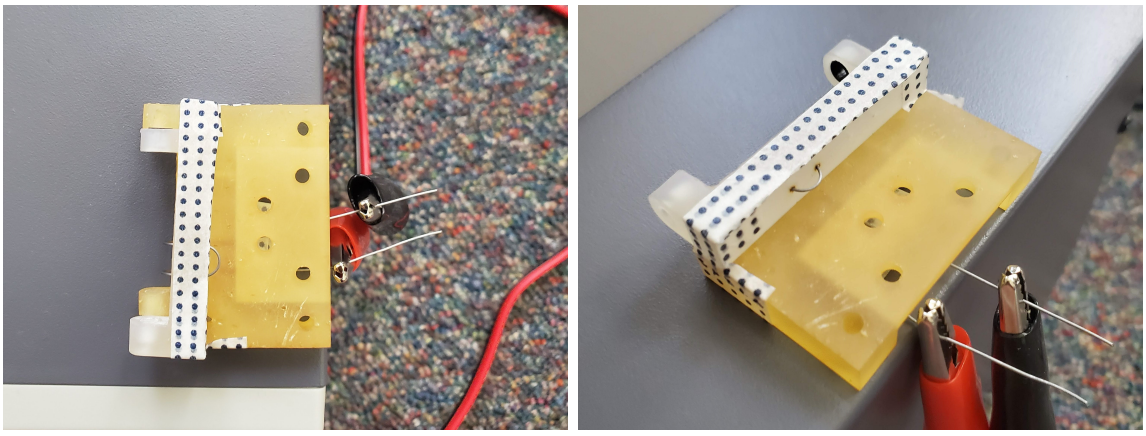

Figure 4-4: Annealing of wire SMA in modified round hinge assembly.

4.3 Round Hinge Prototyping

The round hinge maintained the supported hinge structure, open central cavity, and dual one-way SMA actuators from the flat hinge design with the inclusion of tol-

eranced holes instead of inset channels. The modified hinge structure with round wire actuators is shown in Figure 4-5. The fully enclosed through holes provide less opportunity for buckling in comparison to the open inset channel, where the SMA could bend away from the hinge structure without actuating the hinge. This functions as a fully-enclosed buckling strap by limiting bending to the intended section. The wires were aligned along the neutral axis of the hinge to prevent additional tension or compression.

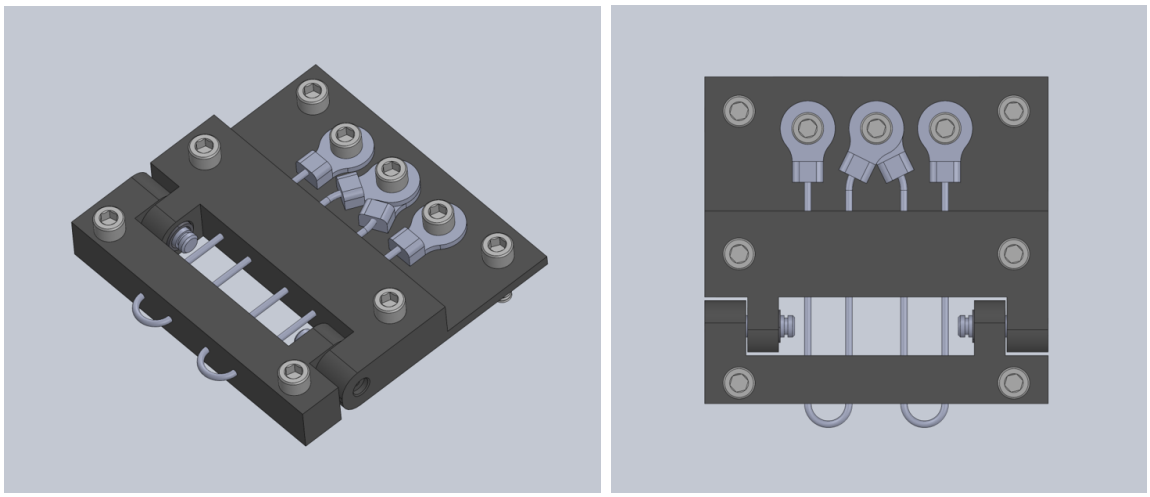

Figure 4-5: Isometric and top views of the round hinge design.

The deployed end of the hinge was shortened to decrease buckling as well. While the loop shape provides some directionality to compensate for the orientation-independent round wire, there is the possibility of torsion of the individual round wires. If both wires rotate within their buckling channels, some actuation force would be in the out-of-plane direction and the total in-plane actuation force would decrease.

Ring terminals were crimped to either end of the SMA actuators in order to establish electrical connections. The ring terminals are bolted to the stationary half of the hinge. The returning end of the SMAs were both bolted to a single contact, functioning similarly to the single copper plate in the flat hinge. There are no external floating wires.

4.3.1 Round Hinge Assembly

The mechanical body of the round hinge was 3D printed out of Formlabs' High Temp Resin on a Form 3 printer, which has a heat deflection temperature of 238 °C and a resolution of 25 microns [73, 74]. All printed components were post-processed in isopropyl alcohol (IPA) for 10 minutes in a Form Wash and cured for 180 minutes at 80 °C in a Form Cure. Given the increased brittleness of the material after the curing process, press fit parts were inserted prior to the Form Cure step [73]. During testing, the higher temperature material effectively prevented the SMAs from melting into the surface of the hinge when heated during actuation. The High Temp Resin provided enough temperature resistance to anneal the actuators without melting.

Electrical connections were implemented with the same bolting mechanism as the flat hinge by using ring terminals crimped onto either end of the actuator. The ends of the SMAs were lightly sanded prior to crimping in order to remove the oxidation layer. It is important to note that hinge modifications are limited in this design due to the inability to remove the SMA after crimping. The integrated round hinge is shown in Figure 4-6. One through channel is slightly burnt due to a rogue step response test where the PWM signal was held at a high duty cycle for an abnormally long period of time.

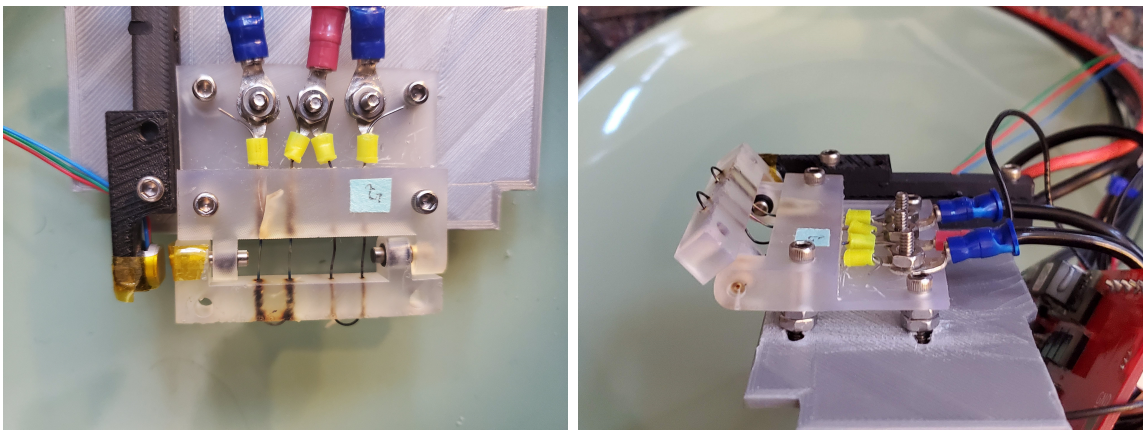

Figure 4-6: Full round hinge prototype.

4.4 Round Hinge Characterization

A plant transfer function of the SMA actuator was modeled by measuring the step response for 5 different duty cycles: 8 DC, 12 DC, 14 DC, 16 DC, and 20 DC. Power and actuation angle were measured for each step response. The output data was filtered using a 200 sample moving-average filter shown for a single trial at 12 DC in Figure 4-7 [62]. Average power was then calculated for each duty cycle: 0.024 W for 8 DC, 0.045 W for 12 DC, 0.059 W for 14 DC, 0.073 W for 16 DC, and 0.097 W for 20 DC. It is interesting to note that the average power for each duty cycle is lower than that of the flat hinge.

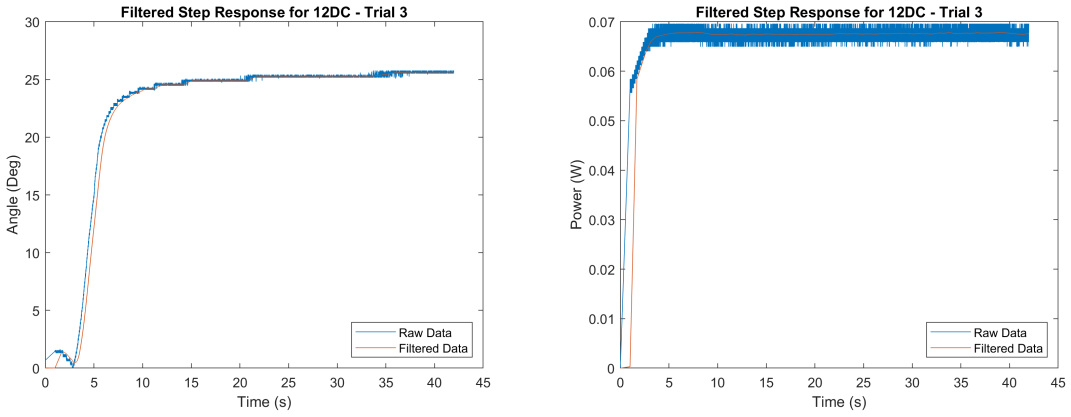

Figure 4-7: Filtered step responses for a single 12 DC run. Script generated by Mario Contreras. [62].

The same step response approach was applied to the round hinge for characterization. Each duty cycle was averaged, artificially elongated according to the final test value, and recorded in Figure 4-8. Outliers with inconsistent rise times and steady state angles were excluded, likely due to accidental preheating of the actuating SMA and insufficient cooling of the opposing SMA. As a whole, the reaction time of the round hinge was approximately twice as fast as the flat hinge.

The transfer function of the round hinge plant was calculated using a pure 2^{nd} order system. While the preheat time was smaller than that of the flat hinge, the addition of pole-zero pairs were investigated to better characterize an observed response lag in the SMA's test data. The initial 2^{nd} order system with 2 poles and

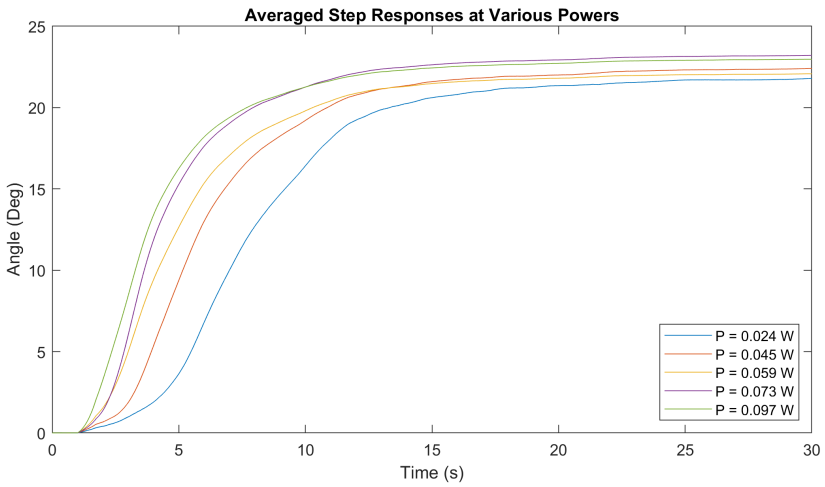

Figure 4-8: Step response output angle with respect to different power levels.

the subsequent filters with additional lags are shown in Figure 4-9. The additional lags provided limited benefit in this case. The final transfer function was determined using the 2nd order system with 2 poles as described by Equation 4.4:

$$\theta(s) = \frac{181.08}{s^2 + 1.344s + 0.5116} \tag{4.4}$$

The step response data for the low operating condition of 12 DC, or 0.045 W, was used to tune the controller gains. Overshoot and response time were driving factors, yielding the following gains: $K_p = 0.0066$, $K_i = 0.0033$, and $K_d = 0.0032$. The step response for the closed loop system is shown in Figure 4-10 with a rise time of 1.8 seconds, a settling time of 5.6 seconds, and an overshoot of 6.3%. When compared to the flat hinge, the round hinge's rise time was twice as fast, the settling time was three times as fast, and the overshoot was comparable.

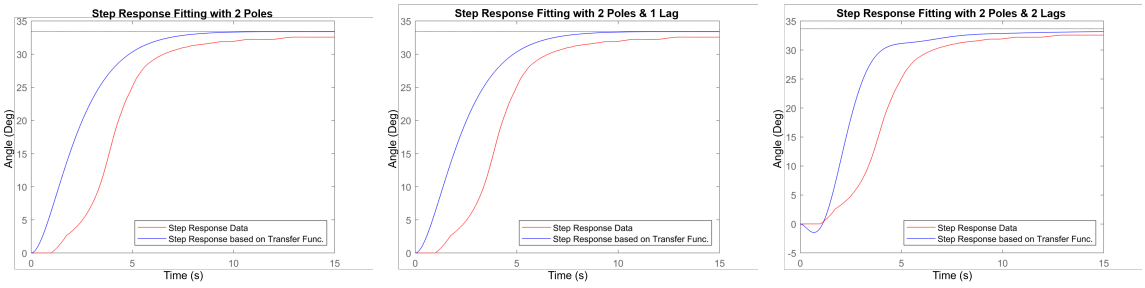

Figure 4-9: Comparison of step response fitting models for 12 DC - Trial 4 data.

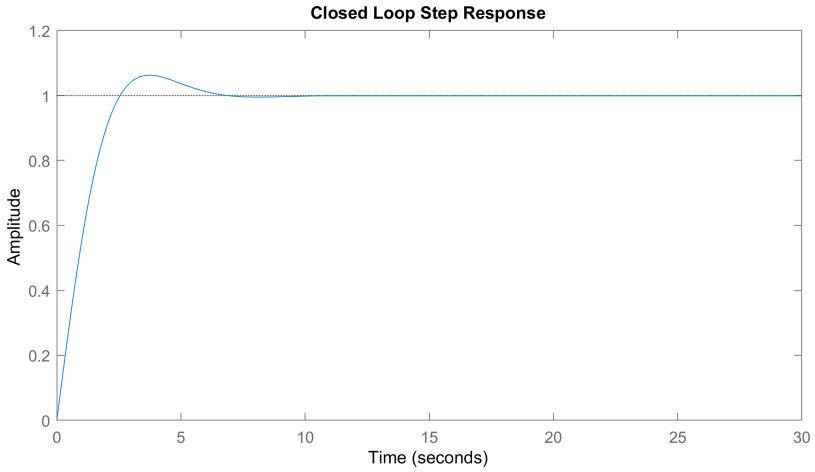

Figure 4-10: Closed loop step response for round hinge.

4.5 Round Hinge Limitations

The primary limitation to the round hinge was the lack of removal method of the SMA actuators. Since the ring terminals were crimped to either end of the wire after threading it through both halves of the hinge, the SMA could not be removed afterwards. The hinge could not be separated or modified either. Any changes would require the actuators to be cut and replaced with new SMA actuators, limiting the ability to reuse SMAs or measure SMA resistances for controls implementation. One potential solution is halving each hinge piece through the center and bolting together the two halves around the loop actuator. Another potential solution is combining the two loop channels into a larger cavity, then adding an insert to divide the channel into two.

The torsion of the SMA wires within their channels was another limitation, further bounding the actuation force in the intended bending direction. Each SMA would rotate as a pair, foreshortening on one end of the loop and elongating on the other to twist the hinge. While the hinge structure prevented torsion beyond each individual loop actuator, the resulting strain did not contribute to the hinge rotation.

Chapter 5

Comparison of Hinge Concepts

Important comparison criteria for the two different FLAPS hinge concepts include actuation range, actuation time, actuation force, and closed loop step response. Ideal actuation range is ±90° per the original solar panel deployment application. Shorter actuation times are preferred for the possibility of quick deployment, though this is not a hard requirement. Actuation force is important with respect to the relative resistance force, ensuring actuation through the desired range of angles. Closed loop step response demonstrates ability to control the hinge and converge to a steady state angle within a prescribed time period. Additionally, the mass and size of the two FLAPS hinges and relevant components are outlined in Table 5.1.

Table 5.1: Size Comparison of Flat and Round Hinge

Component	**Mass (g)**	**Size (cm)**
Flat Hinge	33.94	7.0 x 5.0 x 0.75
Round Hinge	30.63	5.1 x 5.0 x 0.75
CubeSat Cap	37.53	10.0 x 10.0 x 1.8
PCB	164.60	10.0 x 10.0 x 2.5

5.1 Actuation Range

Actuation range was determined using the average steady state angle of each hinge from open loop step response testing. The data for each averaged duty cycle was

elongated to demonstrate a steady state angle as shown in Figure 5-1. The actuation range was bounded by the highest saturation angle achieved by each different hinge design. Using this method, the flat hinge yielded a maximum actuation range of ±18.0°. The round hinge yielded a maximum actuation range of ±23.3°. However, it is important to note that controlled actuation of the flat hinge was demonstrated to an angle of 20.0° during testing, indicating a larger maximum actuation range of ±20.0°.

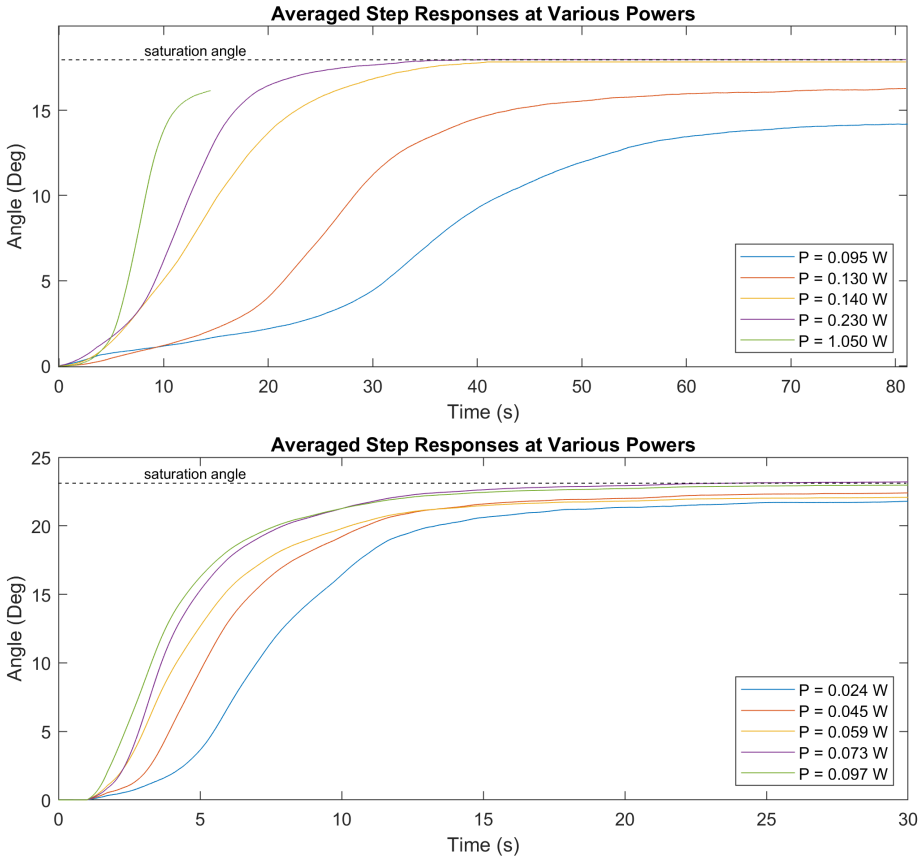

Figure 5-1: Open loop step response. Top: Flat hinge averaged step responses. Bottom: Round hinge averaged step responses.

The calculated difference between actuation force and resistance force indicates that a full 90° is possible. Thus, there must be an additional resistance force limiting the actuation of both hinges. Potential causes include insufficiently overtrained SMAs and buckling.

5.2 Actuation Time

When compared to the open loop response time of the flat hinge in Figure 5-1, the round hinge consistently had a faster actuation time and lower average power. For 20 DC, the round hinge had a power draw of 0.097 W and a settling time of 8.9 seconds, while the flat hinge had a power draw of 0.230 W and a settling time of 19.2 seconds. Moreover, the saturation angle of the round hinge was higher than that of the flat hinge. This means that the round hinge actuated to a further angle in less time at a lower power than the flat hinge.

This might be attributed to the higher resistance of the wire actuator, which results from the smaller cross-sectional area and longer length. To compare the two actuators directly, the round SMA has a calculated resistance of 0.3 Ω compared to the flat actuator's 0.076 Ω. Thus, the round wire will experience more resistive heating than the flat actuator with a lower average input power.

5.3 Hinge Force Calculations

Actuation force was evaluated in order to demonstrate the relationship between input power, actuation angle, and force. Figure 5-2 shows actuation force versus angle traveled for various power inputs to the SMA. Actuation force was calculated using the respective force equation for each of the hinge geometries: Equation 3.1 for the flat hinge and Equation 4.2 for the round hinge. Maximum angle was determined from the step response data of the 5 prescribed duty cycles, where the angle was assumed to be the maximum angle reached at steady state for each trial (Figure 5-1). Thus, Figure 5-2 supports the finding that higher duty cycles result in higher actuation forces and larger steady state maximum angles.

Given the comparable cross-sectional areas and effective actuator lengths, the actuation forces between the two hinge designs are relatively close in value. The difference between the flat hinge actuation force and round hinge actuation force was calculated using Equation 3.1 and Equation 4.2. The actuation forces remained

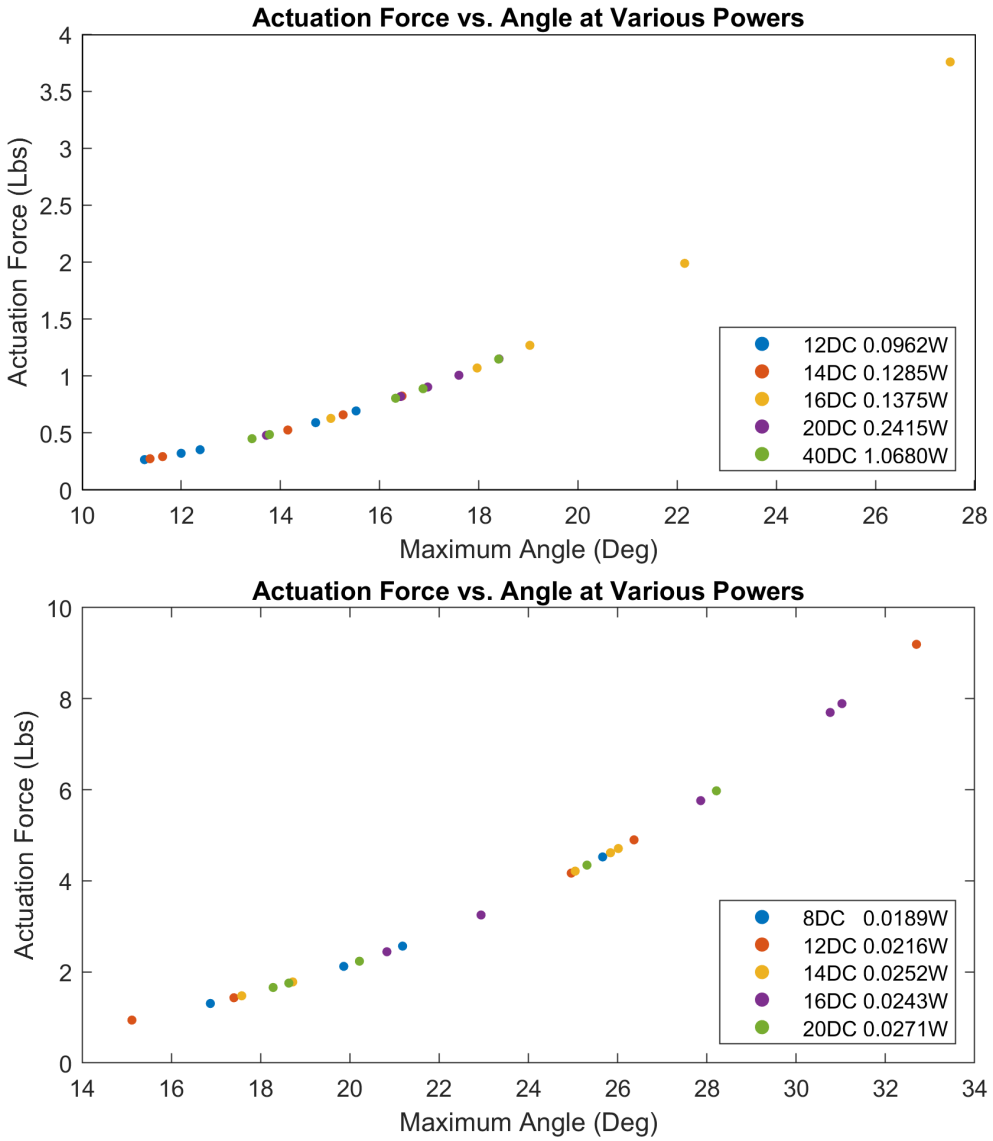

Figure 5-2: Actuation force calculations for varying angles and power levels. Top: Flat hinge actuation. Figure generated by Mario Contreras [60]. Bottom: Round hinge actuation.

within 0.05 lb_f of each other for angles less than 20° and remained within 0.65 lb_f for angles through 45°.

For resistance force, the flat and round hinge values are approximated using the deflection force of a cantilever beam (Equation 2.2). The round actuator's larger second moment of area gives a larger resistance force when compared to the flat hinge. The round actuator's shortened actuator length also increases resistance force, since the deflection of the cantilever changes more quickly with respect to θ. Thus,

the round actuator experiences larger resistance forces overall in comparison to the flat hinge.

When the actuation forces and resistance forces are combined, the net force for both hinges are found to remain close in value. The net force remains within 0.04 lb_f of each other for angles less than 20° and remains within 0.50 lb_f for angles through 45°. Thus, the net force capabilities are very similar over the displacement angles studied.

5.4 Closed Loop Step Response

The simulated closed loop step response shows actuation accuracy with respect to time, as shown in Figure 5-3. Both hinge controllers demonstrate minimal overshoot and quick response times. The rise time of each hinge design mirrors that of the initial step response testing in Figure 5-1, where the response of the round hinge is much faster than the flat hinge. The settling time of both responses, approximately 15 seconds for the flat hinge and 5.6 seconds for the round hinge, fall within the 17 second actuation time requirement stemming from the parabolic flight parameters.

The closed loop testing of the flat hinge met the need for quick actuation with minimal overshoot. This is due to the increased multiplication factors that enabled quicker response times at the expense of larger errors. While both of the described tests had a setpoint of -20°, the factor of 10 gains yielded an actuation time of 75 seconds with an overshoot error of less than 2°. In comparison, the factor of 50 gains had an actuation time of 15 seconds with an overshoot error of less than 3°. Closed loop testing for the round hinge still needs to be completed to validate the simulated results and is not included in this work.

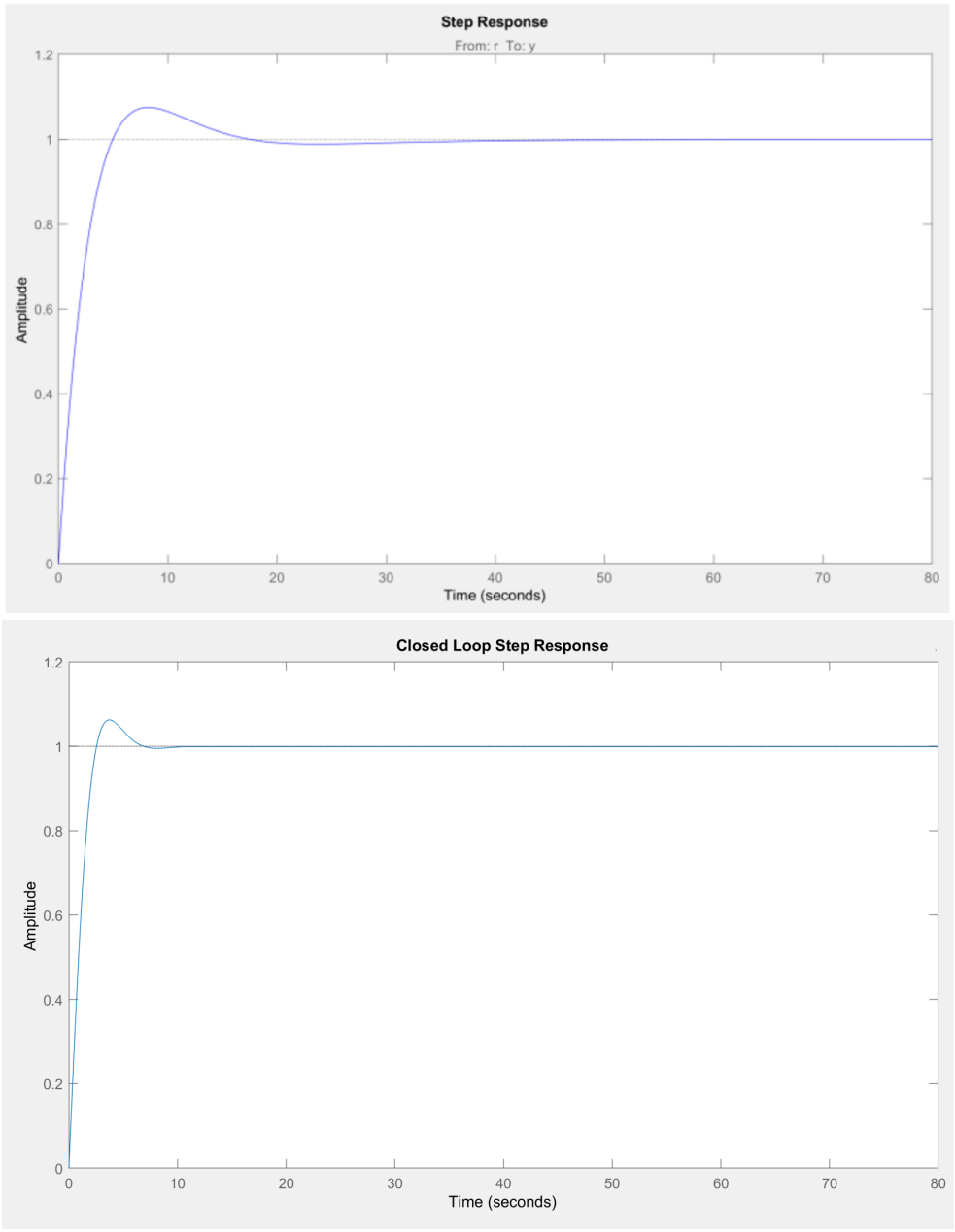

Figure 5-3: Closed loop step responses. Top: Flat hinge response. Figure generated by Mario Contreras [62]. Bottom: Round hinge response.

Chapter 6

Conclusion

This section includes a summary of the results from the flat hinge and round hinge development. Logical next steps are outlined and suggestions for FLAPS integration with a spacecraft are given.

6.1 Summary

This thesis compares the mechanical design, prototype development, and controls implementation for two different SMA hinge architectures: a flat hinge design and a loop hinge design. Overall, the round hinge was able to actuate more quickly with less power, making it attractive for the low SWaP interests of small satellites. Critical comparison values are shown in Table 6.1.

The flat hinge used a rectangular cross-sectioned SMA mounted on either end of a hinge to enable rotary actuation to $\pm 20°$. While step response characterization of the hinge returned an average maximum angle of 18.0°, controlled actuation tests returned angles of 20° and individual step response trials returned angles upwards of 26.7°. Closed loop controller design returned a settling time of approximately 15 seconds with an overshoot of approximately 8%. Closed loop testing yielded an actuation time of 15 seconds with an overshoot of less than 15%, or 3°, when given a -20° setpoint. The hinge was extrusion printed out of Onyx and the SMA actuators were waterjetted out of 80 °C transformation temperature nitinol plates. The SMAs

were oven annealed and quenched.

The round hinge used a circular cross-sectioned SMA mounted to the spacecraft body end of the hinge to enable rotary actuation to ±23.3°. However, individual trials during step response characterization returned actuation angles upwards of 32.7°. The simulated closed loop controller yielded a settling time of 5.6 seconds with an overshoot of 6.3%. The hinge was stereolithography (SLA) printed out of High Temp Resin and the 80°C SMA wire actuators were cut to length with wire cutters. The SMAs were Joule heating annealed and quenched.

Table 6.1: Comparison of Flat and Round Hinge Performance

Property	**Flat Hinge**	**Round Hinge**
Measured Open Loop θ_{max} (°)	18.0	23.3
Measured Closed Loop θ_{max} (°)	20	-
Simulated Closed Loop Actuation Time (s)	15	5.6
Simulated Closed Loop Overshoot (%)	8	6.3

6.2 Next Steps

Short term goals for further development of these hinge concepts include:

- Completing closed loop testing for the round hinge design. The measured actuation time and overshoot error will be compared to the simulated closed loop step response data. This will help validate the model.

- Exploration of additional loop architectures to decrease the actuation time and increase the actuation force exerted by each SMA. Since actuation time is related to the SMA's resistance and actuation force is related to the SMA's cross-sectional area, the geometry of the actuator can be adjusted for those properties.

- Investigating the source of the additional resistance force limiting the actuation range of both hinges. Potential causes include insufficiently overtrained SMAs and buckling.

- Researching the decrease in actuation range of individual SMA actuators over time. This might be attributed to the various annealing methods, annealing parameters, or the continually cycled Joule heating that enables actuation.

- Limiting the SMA buckling demonstrated in each of the hinges. Potential approaches could include adding a degree of freedom in the SMA mounting method or changing the hinge shape in order to avoid overconstraining the actuator.

- Addition of resistance temperature detectors (RTDs) to actively measure SMA temperature, enabling more accurate tracking of the transition from martensite to austenite. Since temperature can be mapped to resistance of the SMA, the controller could generate faster response times without sacrificing accuracy. The RTDs could also prevent accidental re-annealing of the SMAs by cutting power when the SMA approaches the annealing temperature. Alternatively, the RTDs could support temperature monitoring during resistive heating annealing as used for the round hinge.

- Implementing a preheat loop in order to raise the SMA temperature towards A_s prior to actuation. The preheat loop would help minimize controller overshoot caused by low initial temperatures and decrease overall actuation time.

- Lifetime and environmental testing to characterize the performance of each hinge design. Planned tests include failure, fatigue, and thermal vacuum (TVAC) testing. All planned tests are outlined in Appendix B.

6.3 Future Work

Long term considerations in preparation for integration on a spacecraft include:

- Enabling the full $\pm 90^\circ$ actuation range. Large actuation ranges with high precision are the most useful when selecting an in-space rotary actuator. Exploration of alternative SMA hinge concepts might yield larger actuation ranges.

- Evaluating two-way nitinol as a rotary hinge actuator. Training a single two-way actuator to perform the same function as two one-way actuators would decrease the size, mass, and complexity of the hinge structure.

- Evaluating high temperature shape memory alloys (HTSMAs) with transformation temperatures higher than the 140 °C expected from a deployed solar panel. Switching from nitinol with an 80 °C transformation temperature to a HTSMA would help prevent accidental actuation on-orbit.

- Exploring lightweight, space-qualified materials for the hinge body. The current 3D printing process is not suitable for the space environment or vacuum testing, requiring the machining of the hinge structure from a suitable material such as polyetheretherketone (PEEK) or polytetrafluoroethylene (PTFE or Teflon).

- Interface development between the hinge hardware and the host spacecraft. Mechanical, electrical, thermal, and software integration must be outlined and executed.

Appendix A

Force Derivations

This appendix describes the methods used to calculate actuation and resistance force. Figure A-1 shows the assumed geometry. Table A.1 outlines the variables used for flat and round calculations.

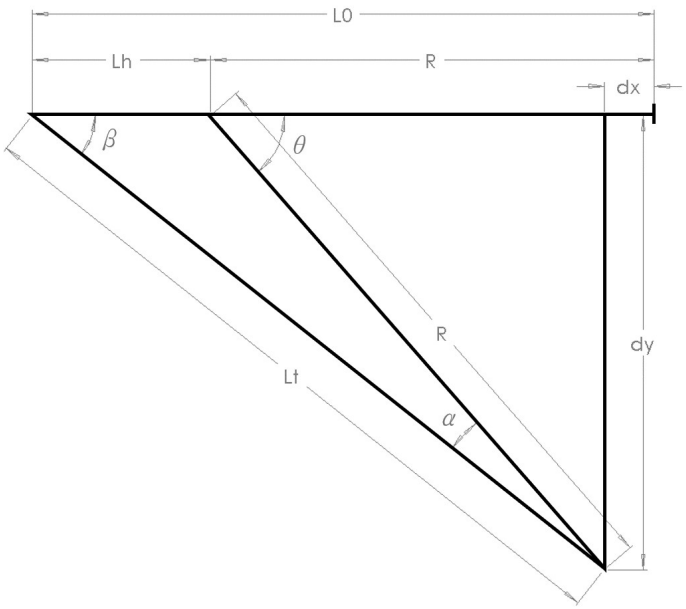

Figure A-1: Approach for calculating forces, as developed by Mario Contreras [62].

Table A.1: Calculation Variables

Property	**Flat Hinge**	**Round Hinge**
Modulus of Elasticity (E) (psi)	6,000,000	6,000,000
Cross-sectional Area (A) (in^2)	0.00078	0.00061
Second Moment of Area (I) (in^4)	0.0026	0.0062
R (in)	1.39	0.73
L_h (in)	0.27	0.17
L_0 (in)	1.66	0.90

A.1 Actuation Force

Due to the buckling strap, the SMA experiences a different bending angle than the angle measured by the encoder. θ represents the angle of the encoder in degrees and β represents the angle of the SMA in degrees. R is the length of the actuator from the encoder to the mounting location in inches, L_h is the length from the buckling strap to the encoder in inches, and L_0 is the length of the actuator from the buckling strap to the mounting location in inches. When the hinge is actuated to angle θ, dx and dy represent the change in location of the mounting location in inches, L_t represents the new length of the actuator in inches, and ΔL is the change in length of the actuator in inches. The force of interest is perpendicular to the encoder instead of the SMA. Thus, α is used to calculate the force in the perpendicular direction in degrees.

$$F_{actuation} = AE\frac{\Delta L}{L_0}\sin\alpha \tag{A.1}$$

$$\Delta L = L_0 - L_t \tag{A.2}$$

$$L_t = \sqrt{(L_h + R\cos\theta)^2 + (R\sin\theta)^2} \tag{A.3}$$

$$\alpha = \theta - \beta \tag{A.4}$$

$$\beta = \tan^{-1} \frac{R \sin \theta}{L_h + R \cos \theta} \tag{A.5}$$

A.2 Resistance Force

The resistance force is approximated as a cantilever beam with the fixed end located at the buckling strap. The free end is the mounting location of the SMA actuator. Deflection (δ) is measured with respect to the rotation of the hinge at the encoder (θ) and the length from the encoder to the mounting location (R). δ is measured in inches, θ is measured in degrees, and R is measured in inches. L_0 is the length from the buckling strap to the mounting location in inches.

$$F_{resistance} = \frac{3EI\delta}{{L_0}^3} \tag{A.6}$$

$$\delta = R \sin \theta \tag{A.7}$$

A.3 Force Plotting

Figure A-2 compares the flat and round actuation, resistance, and net forces.

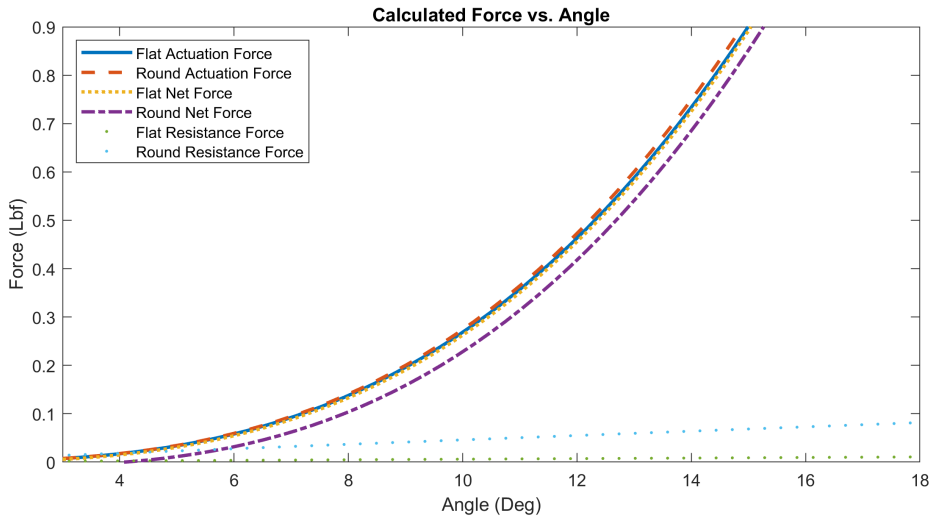

Figure A-2: Comparison of actuation, resistance, and net forces for both hinges.

THIS PAGE INTENTIONALLY LEFT BLANK

Appendix B

Testing Plans

This appendix describes the lifetime and environmental testing planned for characterization of the FLAPS hinges. Table B.1 outlines testing goals. Test interfaces are being developed by the FLAPS test subteam. Facility-dependant testing will commence upon reopening of the necessary labs.

Table B.1: Overview of Test Plan

Objective	**Test(s)**	**Description**
Characterize nominal function	Control	Baseline hinge actuation at ambient temperature and pressure.
Characterize lifecycle	Fatigue, Failure	Characterize the impact of applied stress on hinge function and identify points of failure after extended operation.
Characterize environmental function	Thermal Vacuum	Characterize performance of hinge at in-orbit thermal and vacuum conditions.

B.1 Nominal Testing

Nominal function will be established at ambient temperature and pressure. The hinge will be driven using the closed loop controller with the encoder measuring actuation angle and the RTDs measuring SMA temperature. A camera will record the test for visual inspection. The hinge will be coupled with a back-driven motor to measure torque exerted by the SMA. Test data will be used to derive nominal

maximum actuation angle, nominal maximum actuation torque, and measured torque with respect to actuation angle and power. Testing will take place in STAR Lab.

B.2 Lifecycle Testing

Lifecycle testing will include failure and fatigue testing. For failure testing, the hinge will be actuated using the closed loop controller to the maximum nominal actuation angle. The Arduino will be scripted to cycle between the maximum positive and negative actuation angles. The encoder will measure the actuation angle and the RTDs will measure SMA temperature. A camera will record the test for visual inspection. Exit conditions include failure of the hinge to actuate, degradation of hinge actuation angle to 5° or less, visible damage to the hinge, or 10,000 cycles. Test data will support characterization of the controllable actuation angle with respect to number of cycles and the recorded point of failure. Testing will take place in STAR Lab.

For fatigue testing, the hinge will be driven by the motor coupled to the rotation axis of the hinge. The motor will cycle between maximum positive and negative actuation angles. The magnetic encoder will measure actuation angle and a camera will record the test for visual inspection. After every 1,000 cycles, the hinge will be decoupled from the motor and closed loop control of the hinge will be evaluated. Exit conditions include SMA failure, visible damage to the hinge, or 10,000 cycles. The number of cycles to failure will be recorded for various external torque values. Test data will help evaluate the impact of fatigue on the system over time. Testing will take place in STAR Lab.

B.3 Environmental Testing

Environmental testing will include thermal vacuum (TVAC) testing. The hinge will be mounted to the TVAC chamber with feedthroughs to allow closed loop control via the Arduino. The magnetic encoder will measure actuation angle, the SMA RTDs will measure SMA temperature, and additional RTDs will measure chamber temperature.

Hinge control will first be tested in vacuum at ambient temperature. Recalculation of the controller gains will be performed in order to avoid SMA actuator overheating [57]. The hinge will be actuated through its full nominal actuation range over the temperature range of -90 °C to +90 °C at 15 °C intervals. Exit conditions include failure of the hinge to actuate, visible damage to the hinge, or completion of thermal cycling. Testing will take place in the Space Systems Lab.

THIS PAGE INTENTIONALLY LEFT BLANK

Bibliography

[1] "Nanosats Database." https://www.nanosats.eu, 2020. Accessed: May 15, 2020.

[2] J. Chin *et al.*, "CubeSat 101: Basic Concepts and Processes for First-Time CubeSat Developers," 2017.

[3] "EnduroSat 1U CubeSat Platform." https://www.endurosat.com/cubesat-store/all-cubesat-modules/1u-cubesat-platform, 2020. Accessed: May 15, 2020.

[4] "Innovative Solutions in Space: 1 Unit CubeSat Structure." https://www.isispace.nl/product/1-unit-cubesat-structure, 2020. Accessed: May 15, 2020.

[5] "Blue Canyon Technologies." https://www.bluecanyontech.com, 2020. Accessed: May 3, 2020.

[6] J. Wertz and W. Larson, *Space Mission Analysis and Design*. Space Technology Library, Springer Netherlands, 1999.

[7] T. Prejean, "NanoRacks CubeSat Deployer (NRCSD): Interface Definition Document (IDD)," *NanoRacks*, 2018.

[8] D. Pignatelli *et al.*, "Poly Picosatellite Orbital Deployer Mk. III Rev. E User Guide," *The CubeSat Program*, 2014.

[9] W. K. Belvin, M. Straubel, W. K. Wilkie, M. Zander, J. M. Fernandez, and M. Hillebrandt, "Advanced Deployable Structural Systems for Small Satellites," 2016.

[10] C. Clark and S. Kirk, "Off-the-shelf Deployable Solar Panels for CubeSats," *Clyde Space*, 2018.

[11] "Innovative Solutions in Space: CubeSat Antenna Systems." https://www.isispace.nl/products/cubesat-antenna-systems, 2020. Accessed: May 15, 2020.

[12] R. Hodges *et al.*, "ISARA Integrated Solar Array Reflectarray: Mission Overview," in *27th Annual AIAA/USU Conference on Small Satellites*, 2013.

[13] R. E. Hodges *et al.*, "A Deployable High-Gain Antenna Bound for Mars: Developing a New Folded-Panel Reflectarray for the First CubeSat Mission to Mars," *IEEE Antennas and Propagation Magazine*, vol. 59, no. 2, pp. 39–49, 2017.

[14] "Earth Observation Portal Directory: QuakeSat." https://directory.eoportal.org/web/eoportal/satellite-missions/a/all-star, 2020.

[15] E. Peral *et al.*, "Raincube: A Proposed Constellation of Precipitation Profiling Radars in CubeSat," in *2015 IEEE International Geoscience and Remote Sensing Symposium (IGARSS)*, pp. 1261–1264, IEEE, 2015.

[16] L. Johnson *et al.*, "NanoSail-D: A Solar Sail Demonstration Mission," *Acta Astronautica*, vol. 68, no. 5-6, pp. 571–575, 2011.

[17] G. Thomas *et al.*, "Prototype development and dynamic characterization of deployable cubesat booms," in *51st AIAA/ASME/ASCE/AHS/ASC Structures, Structural Dynamics, and Materials Conference 18th AIAA/ASME/AHS Adaptive Structures Conference 12th*, p. 2907, 2010.

[18] "Oxford Space Systems Technology." https://oxford.space/s-technology, 2020. Accessed: May 16, 2020.

[19] V. Kumar, "Oxford Space Systems Is Developing Massive Space Antennas AstroTube Boom." https://www.rankred.com/oxford-space-systems-antennas-astrotube-boom, 2018.

[20] "STEM Products & Programs STEM (Storable Tubular Extendible Member)," *Northrop Grumman*, 2020.

[21] J. Baker, "AAReST Preliminary Design Review," *California Institute of Technology*, 2013.

[22] "Solar Array Drive Assemblies." https://www.moog.com/products/space-mechanisms/solar-array-drive-assemblies.html, 2020. Accessed: May 17, 2020.

[23] "Sierra Nevada Corporation: Space Technologies Product Catalog 2019." https://www.sncorp.com/media/2725/snc-space-technologies-catalog-2019.pdf, 2019. Accessed: May 17, 2020.

[24] M. Passaretti and R. Hayes, "Development of a Solar Array Drive Assembly for CubeSat," pp. 445–453, 2010.

[25] "MMA Design: Gimbals." https://mmadesignllc.com/products/gimbals/, 2020.

[26] "Earth Observation Portal Directory: QuakeSat." https://directory.eoportal.org/web/eoportal/satellite-missions/q/quakesat, 2020.

[27] M. Obal and T. Barrett, "Aeneas Mission Overview: Lessons Learned," 2014.

[28] "Gunter's Space Page: AlSat-Nano." https://space.skyrocket.de/doc_sdat/alsat-nano.htm, 2017. Accessed: May 17, 2020.

[29] A. R. Sobey and T. R. Lockett, "Design and Development of NEA Scout Solar Sail Deployer Mechanism," 2016.

[30] G. Andersen *et al.*, "FalconSAT-7: A Membrane Photon Sieve CubeSat Solar Telescope," in *Space Telescopes and Instrumentation 2012: Optical, Infrared, and Millimeter Wave*, vol. 8442, p. 84421C, International Society for Optics and Photonics, 2012.

[31] J. F. Sauder *et al.*, "Deployment Mechanisms for High Packing Efficiency One-Meter Reflectarray Antenna (OMERA)," in *AIAA Scitech 2019 Forum*, p. 0755, 2019.

[32] J. Mohd Jani *et al.*, "A Review of Shape Memory Alloy Research, Applications and Opportunities," *Materials and Design*, vol. 56, pp. 1078–1113, 2014.

[33] N. B. Morgan and M. Broadley, "Taking the art out of smart! Forming processes and durability issues for the application of NiTi shape memory alloys in medical devices," in *Materials & Processes for Medical Devices Conference*, ASM International, 2003.

[34] G. Laplanche *et al.*, "Effect of Temperature and Texture on the Reorientation of Martensite Variants in NiTi Shape Memory Alloys," *Acta Materialia*, vol. 127, pp. 143–152, 2017.

[35] M. Follador, M. Cianchetti, A. Arienti, and C. Laschi, "A General Method for the Design and Fabrication of Shape Memory Alloy Active Spring Actuators," *Smart Materials and Structures*, vol. 12, 2012.

[36] A. M. Bassiuny and M. Elsayed, "Identification of Shape Memory Alloy Smart Actuator Using Nonlinear Autoregressive (NARX) Model Identification of Shape Memory Alloy Smart Actuator Using Nonlinear Autoregressive (NARX) Model," December 2014.

[37] M. W. Smith *et al.*, "On-Orbit Results and Lessons Learned from the ASTERIA Space Telescope Mission Conference on Small Satellites," in *32nd Annual AIAA/USU Conference on Small Satellites*.

[38] M. O. Khatsenko, *A Rotary Shape Memory Alloy Actuator for CubeSat Deployable Structures*. Master of Science, Massachusetts Institute of Technology, 2018.

[39] D. E. Hodgson, M. H. Wu, and R. J. Biermannm, *Properties and Selection: Nonferrous Alloys and Special-Purpose Materials*, vol. 2. 1990.

[40] W. Huang, "On the selection of shape memory alloys for actuators," *Materials and Design*, vol. 23, no. June 2000, pp. 11–19, 2002.

[41] J. Kellogg, *Nitinol in Plain Language*. Kellogg's Research Labs, 2020.

[42] E. Patoor *et al.*, "Shape Memory Alloys, Part I: General Properties and Modeling of Single Crystals," *Mechanics of Materials*, vol. 38, no. 5-6, pp. 391–429, 2006.

[43] K. N. Melton, *Ni–Ti based Shape Memory Alloys*. Butterworth-Heinemann, London, 1990.

[44] P. Tautzenberger, "Thermal Actuators: A Comparison of Shape Memory Alloys with Thermostatic Bimetals and Wax Actuators," 1990.

[45] J. Van Humbeeck, "Non-Medical Applications of Shape Memory Alloys," *Materials Science and Engineering: A*, vol. 273, pp. 134–148, 1999.

[46] O. J. Godard, M. Z. Lagoudas, and D. C. Lagoudas, "Design of Space Systems using Shape Memory Alloys," in *Smart Structures and Materials 2003: Smart Structures and Integrated Systems*, vol. 5056, pp. 545–558, International Society for Optics and Photonics, 2003.

[47] "Frangibolt." https://tiniaerospace.com/products/space-frangibolt, 2020. Accessed: May 11, 2020.

[48] "HDRM: Aquimea REACTs." https://arquimea.com/space-hi-rel/mechanisms/hdrm, 2020. Accessed: May 11, 2020.

[49] "Sierra Nevada Corporation: Space Technologies Product Catalog 2015." http://mediakit.sncorp.com/mediastore/document/Space-Technologies-Product-Catalog.pdf, 2015. Accessed: May 11, 2020.

[50] "Mini Frangibolt." https://tiniaerospace.com/products/space-frangibolt, 2020. Accessed: May 11, 2020.

[51] "QWKNUT." http://www.oh1sa.net/data/satellite/cubesat/P-POD-mk2/qwknut3k.pdf, 2020. Accessed: May 11, 2020.

[52] D. A. Hinkley and E. J. Simburger, "Shape Memory Metal Latch Hinge Deployment Method," *The Aerospace Corporation*, 2005.

[53] A. T. Guzik and O. Benafan, "Design and Development of CubeSat Solar Array Deployment Mechanisms Using Shape Memory Alloys," *NASA*, no. June 2018, 2018.

[54] L. Manfredi, Y. Huan, and A. Cuschieri, "Low Power Consumption Mini Rotary Actuator with SMA wires," *Smart Materials and Structures*, vol. 26, no. 11, 2017.

[55] D. E. Hodgson, "Using Shape Memory Alloys," *Shape Memory Alloy Applications*, 1988.

[56] J. P. Swensen, A. M. Dollar, and S. Member, "Optimization of Parallel Spring Antagonists for Nitinol Shape Memory Alloy Actuators," 2014.

[57] J. Fuller, "Shape-Memory Alloy Actuators for Small Satellites," 2017. Accessed: May 4, 2020.

[58] C. Haughwout *et al.*, "FLAPS: Folded Lightweight Aperture Precision System," 2018.

[59] "BeaverCube Preliminary Design Review," *Massachusetts Institute of Technology*, 2018.

[60] P. Do Vale Pereira, *Folded Lightweight Actuated Position System (FLAPS) for CubeSat Deployables*. Master of Science, Massachusetts Institute of Technology, 2019.

[61] J. M. Gere and B. J. Goodno, *Mechanics of Materials*. Cengage Learning, 7th ed., 2009.

[62] M. M. Contreras, K. Cahoy, , and M. Yang, *Design , Analysis , and Control of a Nitinol Shape Memory Alloy Rotary Actuator for Spacecraft Deployable Structures*. Bachelor of Science, Massachusetts Institute of Technology, 2019.

[63] Y. H. Teh, *Fast, Accurate Force and Position Control of Shape Memory Alloy Actuators*. PhD thesis, 2008.

[64] S. Toru, "Fast and Accurate Position Control of Shape Memory Alloy Actuators," 2008.

[65] "ZERO-G Research Program Package: FLAPS," *Zero Gravity Corporation*, 2019.

[66] P. do Vale Pereira, K. Chun, M. Contreras, C. Lindsay, S. Kacker, R. Huffman, C. Haughwout, and K. Cahoy, "FLAPS: Folded Lightweight Actuation Precision System," 2019.

[67] P. do Vale Pereira *et al.*, "Folded Lightweight Actuator Positioning System (FLAPS)," in *33rd Annual AIAA/USU Conference on Small Satellites*, 2019.

[68] M. O. Khatsenko, "FLAPS: Folded Lightweight Aperture Precision System," 2018.

[69] "Kellogg's Research Labs." https://www.kelloggsresearchlabs.com, 2020. Accessed: May 5, 2020.

[70] "OMAX MicroMAX." https://www.omax.com/omax-waterjet/micromax, 2020. Accessed: May 5, 2020.

[71] L. Case *et al.*, "Shape Memory Alloy Shape Training Tutorial," 2004.

[72] "Markforged Material Datasheet: Composites." https://markforged.com/materials/onyx, 2019. Accessed: May 5, 2020.

[73] "Material Data Sheet: High Temp." https://formlabs-media.formlabs.com/datasheets/High_Temp_Technical.pdf, 2018. Accessed: May 5, 2020.

[74] "Formlabs Stereolithography 3D Printers Tech Specs." https://formlabs.com/3d-printers/form-3/tech-specs, 2020. FormLabs.